REPORT DOCUMENTATION PAGE

The public reporting burden for this collection of information is estimated to average 1 hour per response, including the time for reviewing instructions, searching existing data sources, gathering and maintaining the data needed, and completing and reviewing the collection of information. Send comments regarding this burden estimate or any other aspect of this collection of information, including suggestions for reducing the burden, to Department of Defense, Washington Headquarters Services, Directorate for Information Operations and Reports (0704-0188), 1215 Jefferson Davis Highway, Suite 1204, Arlington, VA 22202-4302. Respondents should be aware that notwithstanding any other provision of law, no person shall be subject to any penalty for failing to comply with a collection of information if it does not display a currently valid OMB control number. **PLEASE DO NOT RETURN YOUR FORM TO THE ABOVE ADDRESS.**

1. REPORT DATE (DD-MM-YYYY)	2. REPORT TYPE	3. DATES COVERED (From - To)
January 18th, 2011	Final Technical Report	June 1st, 2007 - October 31st, 2010

4. TITLE AND SUBTITLE		
Creation of Scalable, Cartridge-Based Microreactor Reformers	**5a. CONTRACT NUMBER**	N/A
	5b. GRANT NUMBER	N00014-07-1-0828
	5c. PROGRAM ELEMENT NUMBER	N/A

6. AUTHOR(S)		
Wilhite, Benjamin A.	**5d. PROJECT NUMBER**	N/A
Moreno, Angela M.		
Kim, Daejin	**5e. TASK NUMBER**	N/A
Honda, Gregory H.		
Webb, Benjamin.	**5f. WORK UNIT NUMBER**	N/A

7. PERFORMING ORGANIZATION NAME(S) AND ADDRESS(ES)	8. PERFORMING ORGANIZATION REPORT NUMBER
University of Connecticut 438 Whitney Road Extension, Unit 1133 Storrs, CT 06269-1133	N/A

9. SPONSORING/MONITORING AGENCY NAME(S) AND ADDRESS(ES)	10. SPONSOR/MONITOR'S ACRONYM(S)
	ONR
	11. SPONSOR/MONITOR'S REPORT NUMBER(S) N/A

12. DISTRIBUTION/AVAILABILITY STATEMENT

No distribution limitations apply to public availability of the attached report.

13. SUPPLEMENTARY NOTES

14. ABSTRACT

This report details the design, fabrication and testing of a new class of micro-channel reactors, combining benefits of (i) micromachining for realizing complex, two-dimensional radial distribution patterns for heat transfer and process intensification, and (ii) extrusion for versatile fabrication of scalable micro-channel networks over a range of thermal, mechanical and catalytic properties not currently achievable by current microreactor fabrication methods. This research effort resulted in the successful development of a new class of compact, cost-effective ceramic microreactors for thermal integration. The combination of materials selection and integration architecture enables unparalleled manipulation of three-dimensional thermal profiles for enhancing heat integration in microchemical systems. Experimental efforts demonstrated the ability to realize axial self-insulation with stable thermal gradients in excess of 300oC, with radial thermal profiles in excess of 100oC. In the absence of external insulation of any kind, hydrogen yields of 30% were achieved. Further refinements in system insulation, combustion flame mitigation and distributor designs are expected to

15. SUBJECT TERMS

Fuels reforming; Microreactors; Heat exchange; Process Integration

16. SECURITY CLASSIFICATION OF:			17. LIMITATION OF ABSTRACT	18. NUMBER OF PAGES	19a. NAME OF RESPONSIBLE PERSON
a. REPORT	b. ABSTRACT	c. THIS PAGE			Benjamin A. Wilhite
UU	UU	UU	UU	54	**19b. TELEPHONE NUMBER** (Include area code) 979-845-0406 / 860-810-7309

20110131319

Contract Information

Contract Number	N000140710828
Title of Research	Creation of Scalable, Catridge-Based Microreactor Reformers
Principal Investigator	Benjamin A. Wilhite
Organization	University of Connecticut

Technical Section

1. Overview

The proposed work aims to design, fabricate and test a new class of micro-channel reactors, combining benefits of (i) *micromachining* for realizing complex, two-dimensional radial distribution patterns for heat transfer and process intensification, and (ii) *extrusion* for versatile fabrication of scalable micro-channel networks over a range of thermal, mechanical and catalytic properties not currently achievable by current microreactor fabrication methods. This hybridization of two separate technologies will produce a new class chemical reactor capable of coupling three or more separate kinetic and transport processes within a single cartridge-based unit, thus providing a breakthrough in the design of portable fuel reformers capable of efficiently converting logistics fuels to hydrogen. Product hydrogen can then be employed by next-generation electrochemical engine (fuel cell) systems at efficiencies significantly greater than conventional combustion engine systems.
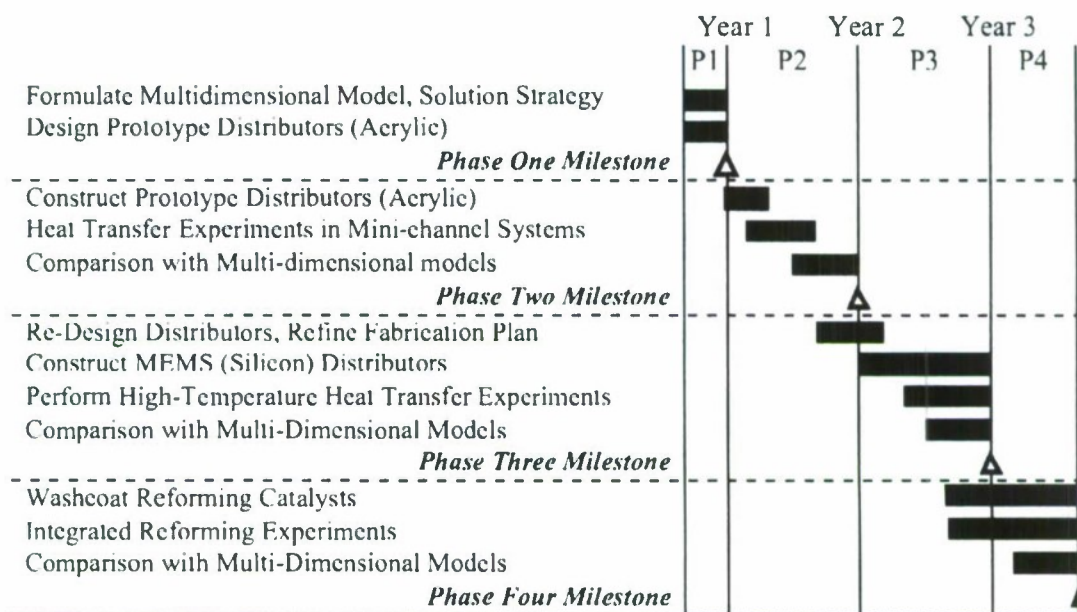
Reforming of logistics fuels to hydrogen for subsequent utilization in a fuel cell system is comprised of multiple physical and chemical processes, including fuel vaporization, contaminant removal and high-temperature reforming stages. The need for autothermal operation (in the absence of external heat addition, common to portable applications) typically requires additional exothermic reactions (e.g. combustion) to provide sufficient heat to maintain required reforming temperatures and supply vaporization heat. The ceramic microchannel network developed by the PI provides a powerful tool for coupling all of these separate transport and kinetic processes within one single cartridge-based, highly efficient reforming unit.

2. Technical Objectives

The proposed research aimed to investigate the influence of radial and axial heat transport in micro-channel networks, for developing a new class of integrated, portable logistics fuel reformers. The proposed timeline of research activities and objectives is presented in Table I, and was organized to produce the following specific deliverables, targeted for the end of each funding period.

- **Months 1-3:** Development of multi-fluid model and simulation strategies for process integration schemes; construction of experimental apparatus. (**Period One**).
- **Months 4-15:** Construction and testing of acrylic-packaged prototype systems for heat exchange between two and three fluids, and comparison with multidimensional modeling of solid-phase heat conduction (**Period Two**).
- **Months 16-27:** Construction and testing of silicon-packaged monolith for heat exchange between two and three non-reacting flows, and comparison with multidimensional modeling of solid-phase heat conduction (**Period Three**).
- **Months 28-36:** Demonstration of the silicon-packaged monolith for two- and three coupled processes, and comparison with multidimensional modeling (**Period Four**).

Table 1: Project Timeline.

	Year 1		Year 2	Year 3
	P1	P2	P3	P4
Formulate Multidimensional Model, Solution Strategy	▬			
Design Prototype Distributors (Acrylic)	▬			
Phase One Milestone	△			
Construct Prototype Distributors (Acrylic)		▬		
Heat Transfer Experiments in Mini-channel Systems		▬		
Comparison with Multi-dimensional models		▬		
Phase Two Milestone			△	
Re-Design Distributors, Refine Fabrication Plan			▬	
Construct MEMS (Silicon) Distributors			▬	
Perform High-Temperature Heat Transfer Experiments			▬	
Comparison with Multi-Dimensional Models			▬	
Phase Three Milestone				△
Washcoat Reforming Catalysts				▬
Integrated Reforming Experiments				▬
Comparison with Multi-Dimensional Models				▬
Phase Four Milestone				▲

3. Progress Statement Summary

Funding of the proposal effort was initiated 07/01/2007. As of 10/31/2010, all objectives have been completed. The primary outcomes of the funded effort are:

- Development of a new approach to creating thermally-integrated ceramic microreactors.
- Experimental demonstration of axial (1-D) self-insulation via materials selection.
- Theoretical validation of axial (1-D) self-insulation using multi-fluid models.
- Experimental demonstration of radial (2-D) thermal integration via architecture selection.
- Establishment of silicon-MEMS construction procedures for further reductions in system weight.

This research effort resulted in the successful development of a new class of compact, cost-effective ceramic microreactors for thermal integration. The combination of materials selection and integration architecture enables unparalleled manipulation of three-dimensional thermal profiles for enhancing heat integration in microchemical systems. Experimental efforts demonstrated the ability to realize axial self-insulation with stable thermal gradients in excess of $300°C$, with radial thermal profiles in excess of $100°C$. In the absence of external insulation of any kind, hydrogen yields of 30% were achieved. Further refinements in system insulation, combustion flame mitigation and distributor designs are expected to be capable of hydrogen yields in excess of 50% under autothermal (self-powered) operation.

In summary, this work provides the groundwork for the continued development and refinement of thermally-integrated systems to achieve further breakthroughs in system efficiency and energy densities. Detailed presentation of all research results is provided in Section 5.

4. Research Outcomes & Discussion

4.1 Objectives for Period One (06/01/07 – 09/30/07):

- Formulate multi-fluid model, solution strategy
- ototype distributors (Acrylic)

        evelopment

Multi-fluid models were developed for analyzing the influence of fluid and solid-phase thermal properties, reaction kinetics, thermodynamics, and packaging conditions (adiabatic/insulating or isothermal/uninsulating) upon thermal efficiency and reaction progression ed endo- and exothermic process streams. In this section, model derivations are detailed.

A general pseudo-homogeneous, one-dimensional steady-state model is developed to describe plug-flow in two parallel microchannels separated by an impermeable wall, shown in Figure 1.The model assumes incompressible flow and neglects mass transfer limitations between catalyst and fluid and internal diffusion limitations within the catalyst phase. A unique fluid is supplied to each channel at fixed velocity ($u_{i=1,2}$) and inlet temperature ($T_{i=1,2}$) in either co- or counter-current configuration. Each fluid experiences chemical reaction and/or heat transfer with the dividing wall. The dividing wall in turn exchanges heat with both fluids, and also with its surround via packaging conditions at either end of the device.
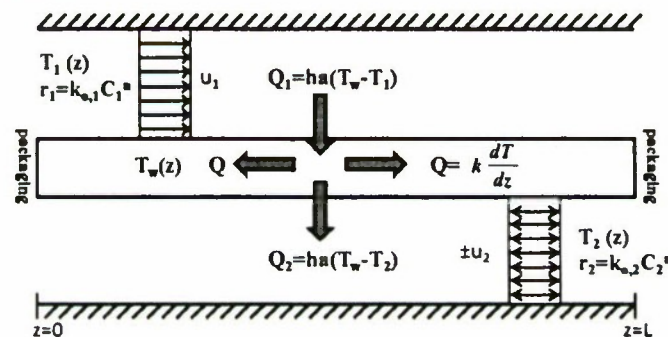
Figure 1: Schematic of simplified one-dimensional model describing heat transfer between two parallel microchannels with solid-phase heat conduction in axial direction

This preliminary study concentrates solely upon the effect of solid-phase heat dispersion on heat transfer efficiency; the further assumption of negligible axial dispersion is also employed. The steady-state energy balance governing each fluid thus accounts for heat generated via chemical reaction, heat transfer between fluid and the solid wall. (Equation 1.1)

$$\pm \frac{dT_i}{dz} = \frac{h_i a_i}{\rho_i u_i Cp_i}\left(T_w - T_i\right) + \frac{k_{o,i}C_i^n\left[-\Delta H_{rxn,i}\left(T_i\right)\right]}{\rho_i u_i Cp_i}\exp\left[\frac{-Ea_i}{RT_i}\right] \tag{1.1}$$

The mass balance for fluid i, accounting for a simplified irreversible, power law kinetic reaction in the absence of mass transfer limitations and with axial convection in either co- or counter-current operation is given by Equation 1.2:

$$\pm \frac{dC_i}{dz} = r_A = -k_{0,i}C_i^n\exp\left[\frac{-Ea_i}{RT_i}\right] \tag{1.2}$$

The resulting one-dimensional model describing the dividing wall accounts for axial thermal conduction and heat addition/removal by the two fluid-phases (Equation 3):

$$\frac{d^2T_w}{dz^2} = \sum_{i=1}^{N}\frac{h_i d_i}{k_w A_w}\left(T_w - T_i\right) \tag{1.3}$$

The influence of packaging upon heat dissipation is modeled by appropriate selection of boundary conditions for the solid-phase. This analysis considers the two ideal cases of (i) isothermal and (ii) adiabatic packaging of the microchannel network. Isothermal boundary conditions assume that the wall temperature is fixed at either extrema. For counter-current systems, wall temperatures are assumed equal to the corresponding inlet fluid temperature at each extrema. For co-current systems, wall temperatures are assumed equal to the weighted-average temperature of the two fluids at each extrema. Adiabatic conditions assume that the first derivative of the wall temperature at each extrema is fixed and equal to zero. In general, the isothermal and adiabatic boundary conditions may be written as:

$$T_w \equiv \text{fixed @ z=0, L} \tag{1.4a}$$

$$\frac{dT_w}{dz} = 0 \text{ @ z = 0, L} \tag{1.4b}$$

Temperature, concentration and position within the microchannel network are rendered dimensionless as follows:

$$\theta_i = \frac{T_i(z) - T_{min}}{T_{max} - T_{min}}; Y_i = \frac{C_i(z)}{C_{i,o}}; \tilde{z} = \frac{z}{L} \tag{1.5}$$

The dimensionless temperature θ_i is defined in terms of the maximum and minimum achievable temperatures within the heat-exchanger system. The resulting dimensionless expressions for M fluids exchanging heat through a single, radially uniform wall are

$$\pm \frac{dY_i}{d\tilde{z}} = -Da_i Y_i^n\exp\left[\frac{-Ea_i}{RT_i}\right] \tag{1.1'}$$

$$\pm\frac{d\theta_i}{d\bar{z}} = NTU_i\left(\theta_w - \theta_i\right) + \left(\frac{\gamma_i}{\gamma_1}\right)Da_iY_i\exp\left[\frac{-\alpha_i}{1+\gamma_i\theta_i}\right] \qquad (1.2')$$

$$\frac{d^2\theta_i}{d\bar{z}^2} = \sum_{i=1}^{M}\frac{NTU_i}{CP_i}\left(\theta_w - \theta_i\right) \qquad (1.3')$$

From Equation 1.2', the kinetics of the ith reacting fluid is described by Damkohler number, (Da_i), dimensionless activation coefficient (α_i) and dimensionless heat of reaction (γ_i). Fluid-solid heat transfer is described by the number of transfer units (NTU_i), while the solid-phase axial conduction is described by the conduction parameter (CP_i), following previous analysis of non-reacting fluids by Peterson (1999) and Stief and coworkers (1999). Value ranges for each parameter were estimated based upon typical microchannel dimensions and different solid-phase material properties. Fluid-solid heat transfer coefficients are estimated assuming gas phase, while fluid-solid heat transfer coefficients are estimated from the correlations of Sieder and Tate (Geankoplis, 2003). Details of parameter space estimation are presented in Table 1.1.

Isothermal boundary conditions allow pinning the wall temperature at either boundary, i.e. the packaging-microchannel interface, allowing free heat exchange between the microchannel solid-phase and the packaging layers. These conditions correspond to the limiting case of packaging with high thermal conductivity materials (e.g. silicon) which allow thermal equilibration between the packaging layer and the inlet fluid. Solution requires determination of heat flux between packaging layer and solid-phase at the lower boundary or initial condition ($z=0$) that satisfies target isothermal temperature at the upper boundary ($z=L$). For the case of counter-current operation, this upper-bound wall temperature is equal to the inlet temperature of counter-current flow. For co-current operation, the upper boundary wall temperature is equal to the mass averaged temperature of the two exiting fluids. Adiabatic boundary conditions assume zero heat flux between the packaging and the microchannel network, in turn allowing solid-phase wall temperatures to be driven purely by heat exchange between the two fluids. These conditions correspond to the limiting case of packaging with thermally insulating materials. Solution requires determination of lower boundary wall temperature to satisfy the zero flux condition at the upper boundary, independent of fluid temperatures.

4.1.1.1. Modeling Analysis, Case I: Microscale Heat Exchanger

The simplest case of the general model is the steady state heat exchange between two fluids in absence of any chemical reaction (α_i, $Da_i = 0$). The resulting system of equations is cast solely in terms of the number of transfer units (NTU) and fluid conduction parameter (CP).

$$\frac{d\theta_1}{d\bar{z}} = NTU_1\left(\theta_w - \theta_1\right) \qquad (1.6)$$

$$\frac{d\theta_2}{d\bar{z}} = NTU_2\left(\theta_w - \theta_2\right) \qquad (1.7)$$

$$\frac{d^2\theta_w}{d\bar{z}^2} = \frac{NTU_1}{CP_1}\left(\theta_w - \theta_1\right) + \frac{NTU_2}{CP_2}\left(\theta_w - \theta_2\right)$$

(1.8)

The heat exchanger effectiveness, ε, is calculated from the resulting temperature profile as follows:

$$\varepsilon = \frac{T_2\big|_{z=0} - T_2\big|_{inlet}}{T_1\big|_{inlet} - T_2\big|_{inlet}} = \theta_2$$

(1.9)

Additionally, for the isothermal case, the ratio of conductive (solid-phase) to convective (fluid-phase) heat losses can be obtained from Equation 1.10, as originally shown by Peterson (1999):

$$\lambda = CP\frac{\left(d\theta_w/d\bar{z}\right)\big|_{\bar{z}=1}}{\theta_1\big|_{\bar{z}=1}}$$

(1.10)

Results obtained for the case of isothermal packaging conditions are presented in Figure 2.
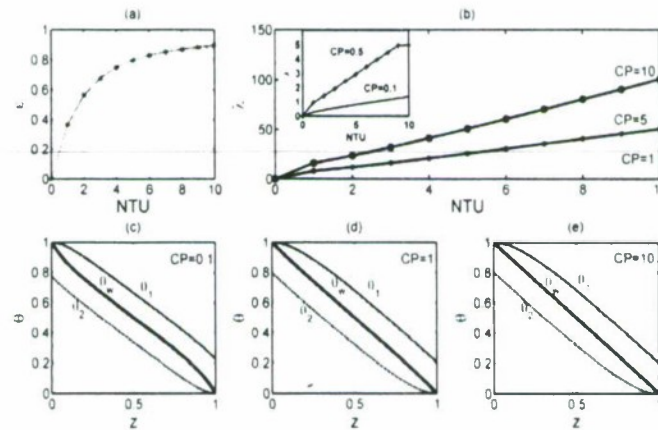
Figure 2: Heat Exchanger Simulation Results, for Isothermal Packaging Conditions: (a) effectiveness and (b) conduction losses as a function of NTU and CP; corresponding thermal profiles for NTU=5 at (c) CP=0.1, (d) CP=1, (e) CP=10

Heat exchanger efficiencies and conduction losses over a range of NTU are presented for the cases of low, intermediate and high solid-phase thermal conductivities in Figure 2a, with corresponding temperature profiles of the solid and both fluid-phases in Figure 2-e for NTU=5. As seen in Figure 2a, the effectiveness is a weak function of the conduction parameter. However, as CP increases, substantial increases in conduction heat losses occur. For this isothermal case, the effectiveness is held at high values despite increasing conduction losses with increasing CP, because the wall temperature is pinned by external conditions. These results

clearly demonstrate the benefit of employing intermediate thermal conductivity wall materials to maintain rapid heat transfer while minimizing conductive heat losses via packaging.

Results obtained for the case of adiabatic packaging conditions are presented in Figure 3. Efficiencies are presented for the cases of low, intermediate and high solid-phase thermal conductivities in Figure 3a. Heat exchanger effectiveness is significantly reduced with increasing CP, despite the removal of conductive heat losses (via adiabatic packaging conditions). This can be understood by examining the corresponding temperature profiles of the solid and fluid-phases presented in Figure 3b-d for NTU=5. As CP increases the system approaches the limit of thermal equilibration between the two fluids and the wall, equivalent to co-current operation, and in turn imposing a maximum efficiency of 50%. Conversely, low thermal conductivity materials allow maintenance of substantial thermal gradients along the solid-phase axial length by preventing thermal equilibration.
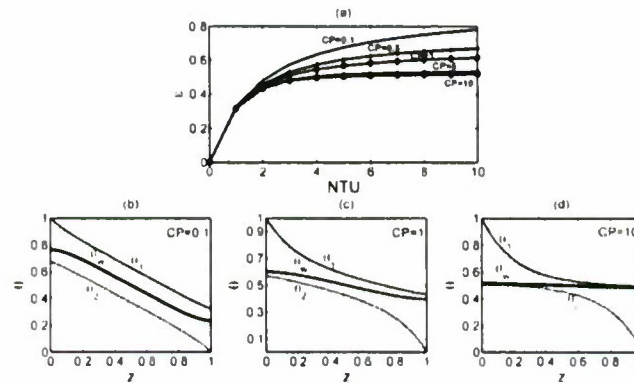
Figure 3: Results for Adiabatic Microscale Heat Exchanger: (a) effectiveness as a function of NTU and CP; corresponding thermal profiles for NTU=5 at (b)CP=0.1, (c)CP=1, (d)CP=10

In both cases, the effectiveness is a weak function of CP at low NTU where the solution is dominated by the NTU, and under isothermal conditions the effectiveness is dominated by CP at large NTU owing to accumulated conduction losses.

4.1.1.2. Modeling Analysis, Case II: Microscale Regenerative Combustor

The analysis is extended to the case of one exothermic reacting fluid exchanging heat with a second non-reacting fluid via the solid-wall, for the case of an irreversible first order reaction. Both fluids are assumed to enter the system at identical temperatures in order to isolate the exothermic reaction as the sole heat source in the system. With this condition, the minimum temperature achievable in the system becomes the coolant/reactant inlet temperature ($T_{min}=T_{1,inlet}$) while the maximum theoretical fluid temperature is obtained solely from the adiabatic temperature rise of the exothermic reaction. Equations 1'-3' are rewritten as follows:

$$\frac{dY_i}{d\bar{z}} = -Da_1 Y_1 \exp\left[\frac{-\alpha_1}{1+\gamma_1\theta_1}\right] \tag{1.11}$$

$$\frac{d\theta_1}{d\bar{z}} = NTU_1\left(\theta_w - \theta_1\right) + Da_1 Y_1 \exp\left[\frac{-\alpha_1}{1+\gamma_1\theta_1}\right] \tag{1.12}$$

$$\frac{d\theta_2}{d\bar{z}} = NTU_2\left(\theta_w - \theta_2\right) \tag{1.13}$$

$$\frac{d^2\theta_w}{d\bar{z}^2} = \frac{NTU_1}{CP_1}\left(\theta_w - \theta_1\right) + \frac{NTU_2}{CP_2}\left(\theta_w - \theta_2\right) \tag{1.14}$$

Equations 11-14 allow to study the effects of design (NTU, CP) and kinetic parameters (α, γ, Da) alongside both adiabatic and isothermal conditions on system performance. This is cast in terms of reaction conversion and system thermal efficiency, the latter defines as:

$$\varepsilon = \frac{T_2\big|_{\bar{z}=0} - T_2\big|_{inlet}}{T_{max} - T_{min}} = \frac{T_2\big|_{\bar{z}=0} - T_2\big|_{inlet}}{\Delta T_{ad}} = \theta_2 \tag{1.15}$$

In order to investigate the effect of NTU and CP on system thermal efficiency and reactor conversion for both the isothermal and the adiabatic packaging, a set of "mild" kinetic parameters are initially employed ($\gamma=2$, $\alpha=10$).
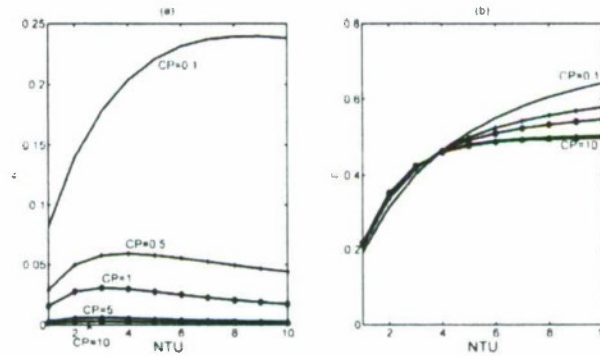
Figure 4: Results of Regenerative Combustion Simulations; (a) isothermal packaging conditions; (b) adiabatic packaging conditions.

Figure 4 represents a parametric study varying CP and NTU for both packaging conditions. CP is varied from 0.1 to 10 over a range of NTU's, to simulate a wide selection of solid-phase thermal conductivities. A sufficient value of the Damkohler number is employed to ensure complete conversion in the absence of steady-state multiplicity (Moreno, et al. 2008). Results in

Figure 4a clearly show that the effectiveness is a strong function of the conduction parameter for the isothermal case, unlike the heat exchanger case discussed in Figure 2. This difference can be understood by examination of the wall boundary conditions. In the heat exchanger analysis, wall temperatures are fixed equal to fluid inlets; i.e. the driving force for heat transfer is defined solely by the boundary conditions, not by the system. For reacting fluid analysis, wall boundary temperatures are fixed corresponding to identical inlet temperatures, such that the exothermic reaction (occurring within the system) is the sole driving force for heat transfer. Increasing NTU over the range of ~0-5 results in increasing effectiveness regardless of CP, while further increases in NTU result in reduced effectiveness, as conduction losses accumulate.

Figure 4b shows the results for the effect of CP and NTU on the adiabatic heat exchanger reactor. At low NTU, the effectiveness is a weak function of the conduction parameter in the absence of conduction losses via packaging. However, at high NTU, CP again becomes an important parameter, reflecting the potential for localized heat accumulation in the solid-phase (i.e. hot-spot formation). For the remainder of the analysis presented, a value of NTU=5 is assumed, corresponding to a balance between providing sufficient contacting time for heat transfer between fluids and minimizing conduction losses and/or reactor size. The influence of solid-phase wall conduction upon hot-spot formation, steady state multiplicity and thermal efficiency at fixed intermediate values of NTU is studied in detailed (see Moreno et al) for the cases of isothermal and adiabatic packaging conditions, respectively. In both cases, sufficient low solid-phase thermal conduction supports the formation of a localized hot-spot along the solid-phase axial profile, in addition to the expected fluid-phase hot-spot. The effect of thermal conductivity on the system performance and the presence of steady-state multiplicity are also studied. Ignition/extinction behavior is expected, with important implications for microsystem operation. For the case of isothermal packaging, the rate of heat removal from the system via packaging losses increases (independent of convective heat removal), while serves to stabilize the system at the expense of substantial losses. For the case of adiabatic packaging, only the unstable solutions change with conduction parameter, while the range of Da corresponding to multiple steady-states is unaffected by CP. This analysis suggests a design trade-off between reactor stability and competitive thermal efficiencies.

It is important to note that for the case of isothermal packaging and sufficient CP and NTU corresponding to isothermal coolant and solid-phase conditions, the system of equations reduces to a single plug-flow reacting fluid described by an initial-value ordinary differential equation which must yield a unique solution. The introduction of boundary-value equations describing the solid-phase temperature as well as any counter-current flows in turn allows the possibility of multiple steady-states. That the present model, which neglects several established sources of steady-state multiplicity demonstrates multiplicity due solely to packaging and materials selection clearly shows the importance of these two design parameters in the design of thermally-integrated microsystems.

4.1.1.3. Modeling Analysis, Case III: Heat Exchanger Reactor

Lastly, analysis is extended to the coupling of an exothermic reacting fluid with an endothermic reacting fluid. The general model Equations 1'-3' reduce to the following:

$$\frac{dY_1}{d\bar{z}} = -Da_1 Y_1 \exp\left[\frac{-\alpha_1}{1+\gamma_1\theta_1}\right] \tag{1.16}$$

$$\frac{dY_2}{d\bar{z}} = \pm Da_2 Y_2 \exp\left[\frac{-\alpha_2}{1+\gamma_2\theta_2}\right] \tag{1.17}$$

$$\frac{d\theta_1}{d\bar{z}} = NTU_1\left(\theta_w - \theta_1\right) + Da_1 Y_1 \exp\left[\frac{-\alpha_1}{1+\gamma_1\theta_1}\right] \tag{1.18}$$

$$\frac{d\theta_2}{d\bar{z}} = NTU_2\left(\theta_w - \theta_2\right) \pm Da_2 Y_2 \exp\left[\frac{-\alpha_2}{1+\gamma_2\theta_2}\right] \tag{1.19}$$

$$\frac{d^2\theta_w}{d\bar{z}^2} = \frac{NTU_1}{CP_1}\left(\theta_w - \theta_1\right) + \frac{NTU_2}{CP_2}\left(\theta_w - \theta_2\right) \tag{1.20}$$

Thermal efficiencies are calculated based on the heat released from the exothermic reaction that is utilized to (i) drive the endothermic reaction and (ii) as sensible heat; as follows:

$$\varepsilon = \theta_2 + X_2\gamma_2 \tag{1.21}$$

Results from Figure 5 show that system efficiency and stability are complex functions of the effect of conduction parameter. Under isothermal conditions, increasing CP results in losses of thermal efficiency (at sufficient values of the Damkohler number corresponding to complete conversion of the exothermic reacting fluid) due to conduction losses via packaging, as observed in the microscale regenerative combustor case. Under adiabatic conditions, the solutions of very low and very high values of Damkohler number are independent of the conduction parameter, and thermal efficiencies are consistently higher owing to the absence of conductive losses via packaging. In both cases increasing CP results in multiple steady-states for both reacting fluids.
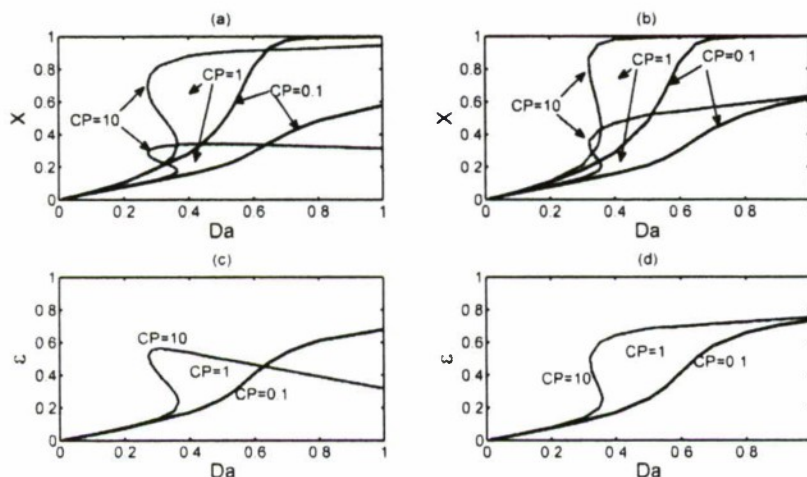
Figure 5: Simulation Results for Co-Current Heat Exchanger Reactor, (a,c) isothermal packaging; (b,d) adiabatic packaging.

Similar analysis for the case of counter-current operation is presented in Figure 6. Comparison of results in Figure 5 (for co-current) and Figure 6 (for counter-current) illustrates the additional influence of flow configuration on both thermal efficiency and multiplicity. While maximum efficiencies are similar for both co- and counter-current flow, Damkohler numbers necessary for complete conversion of the exothermic fluid reduce mildly for the case of counter-current flow, mostly noticeably at low values of the conduction parameter. Multiplicity behavior is similar for both adiabatic cases while counter-current operation removes steady-state multiplicity in the isothermal case.
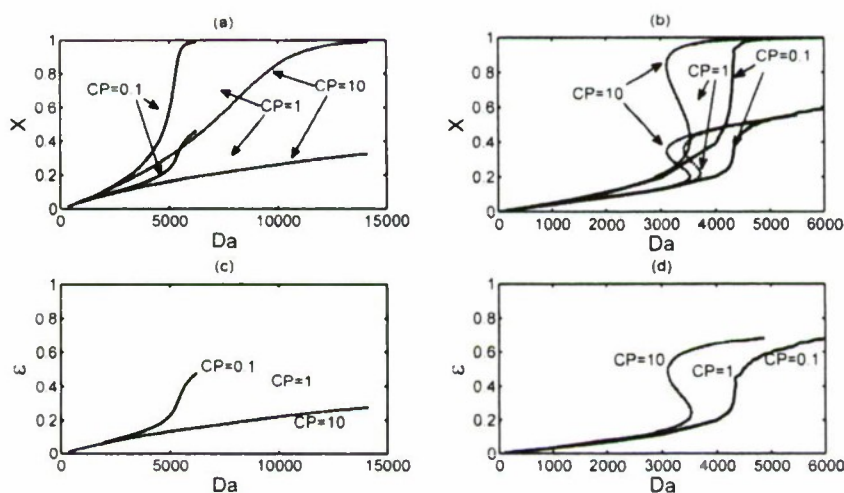
Figure 6: Simulation Results for Counter-Current Heat Exchanger Reactor, (a,c) isothermal packaging; (b,d) adiabatic packaging.

4.1.2. Summary of Modeling Analysis

Modeling analysis indicates that under expected operating conditions and materials selection, heat-exchanger efficiencies of 60 – 80% are predicted for the silicon-packaged ceramic mini-channel system. *Simulations of regenerative-combustion configuration* (exothermic reacting fluid, heat transfer fluid) *predict thermal efficiencies approaching 30% for isothermal packaging conditions, and efficiencies approaching 65% for adiabatic packaging.* These results indicate the need for minimizing heat transfer from the monolith to the packaging materials, either by minimizing interfacial contact area or the use of insulating gasket materials during packaging. *Simulations of heat-exchanger reactor configuration* (exothermic reacting fluid, endothermic reacting fluid) *predict thermal efficiencies approaching 60-70%, albeit with significant light-off or ignition behavior.* Thermal efficiencies are improved, at the expense of magnified ignition behavior, by minimizing heat transfer between the cordierite mini-channel network and the silicon distributors. *Overall, simulations predict promising thermal efficiencies while identifying the factors influencing steady-state multiplicity and ignition/extinction behavior.* Simulations justify the selection of cordierite ceramics as sufficiently low thermal conductivity materials for the proposed effort.

Table 1: Determination of parameter values for microchannel heat transfer model

Fluid Properties	Value
Fluid Density (kg.m⁻³)	1.2
Fluid Viscosity (Pa·s)	1.8×10^{-5}
Fluid Heat Capacity (J.kg⁻¹K⁻¹)	1000
Fluid Thermal Conductivity (W.m⁻¹.K⁻¹)	0.025

Microchannel Properties	Extruded Monoliths			Microfabricated Devices		
Hydraulic Diameter (m)	1.5×10^{-3}			0.5×10^{-3}		
Flow Length (m)	5×10^{-2}			1×10^{-2}		
Surface Area (m²)	3×10^{-4}			2×10^{-5}		
Volume (m³)	1.1×10^{-7}			2.5×10^{-9}		
a (m⁻¹)	2700			8000		
Residence Time (s)	0.01	0.1	1	0.01	0.1	1
Heat Transfer Coefficient (W.m⁻².K⁻¹)	70	32.5	15	101	46.9	21.8
NTU	1.5	7.2	33	6.7	31	144

Substrate Properties								
Thermal Conductivity (W.m⁻¹.K⁻¹)	2	16.5	165	200	2	16.5	165	200
CP	0.007	0.07	0.7	2	0.165	1.65	16.5	2
	0.7	6.61	66	0.165	1.65	16.5	165	1651

4.2. Objectives for Period Two (10/01/07 – 09/30/08):
- Construct Prototype Distributors (Acrylic)
- Distribution Quality and Heat Transfer Experiments in Mini-channel Systems
- Comparison with Multi-dimensional models

4.2.1. Construction of Prototype Distributors

The first prototype distributor has been completed and fully analyzed for fluid distribution and heat-transfer performance. Based upon findings on distribution quality, additional pressure-drop constrictions were incorporated into all three designs.
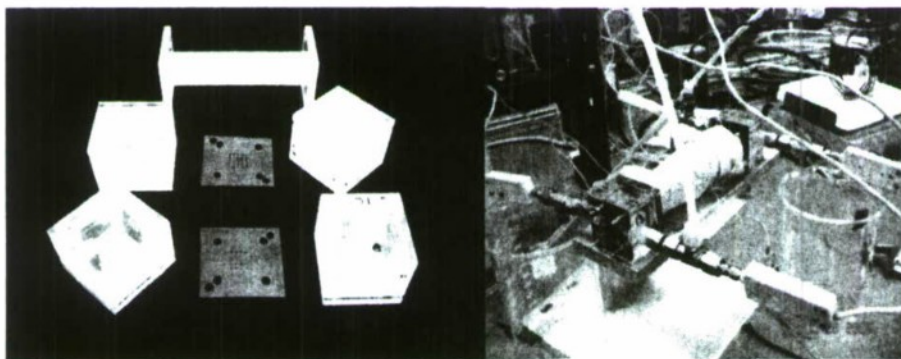
Figure 7: Checkerboard acrylic prototype for two-fluid integration

4.2.2. Distribution Quality Measurements Using Mini-channel System

4.2.2.1. Residence Time Distribution. Liquid-Phase Flow

Residence time distributions were obtained using the experimental apparatus and prototype distributor (Figure 7b). Residence time distributions were determined experimentally by tracer injections of aqueous blue dye solutions into the reactor. Absorbance measurements in the effluent stream are taken as a function of time using a UV-Vis spectrophotometer and flow-through cuvette at a constant wavelength of 430 nm. The absorbance vs. time profiles were obtained for: i) Flow through a single cordierite channel, ii) 5x5 microchannel reactor with tracer injection through 12 channels, iii) 5x5 microchannel reactor with tracer injection through 13 channels.
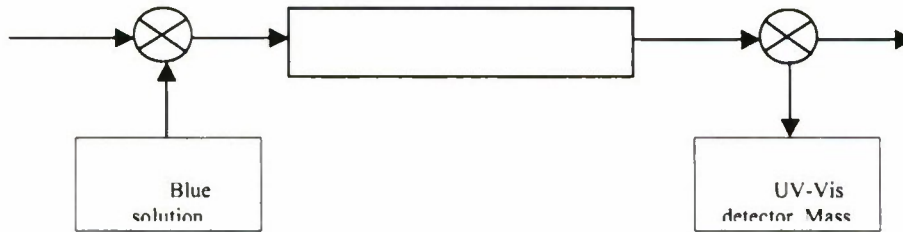
Figure 8: Schematic representation of the RTD analysis

The Beer-Lambert law states that the absorbance of a solution is directly proportional to the solution's concentration. Thus UV/VIS absorbance readings can be used to determine the concentration of a solution.   Under the assumption that The Beer-Lambert law applies, the absorbance profiles can be directly used to calculate the Residence Time Distribution function, $E(t)$, (see Equation 2.1) as follows:

$$E(t) = \frac{C(t)}{\int_0^\infty C(t)dt} = \frac{A(t)}{\int_0^\infty A(t)dt} \tag{2.1}$$

Where A is the measured absorbance, $C(t)$, is the concentration of the blue dye solution with time and F, is the constant of proportionality and is calculated based on the molar absorptivity and the length of light path through the cuvette. This factor F is assumed to be constant through the experiment.

The first and second moments of the RTD, or the mean value and the variance, respectively are calculated as follows:

$$\tau = \frac{\int_0^\infty tE(t)dt}{\int_0^\infty E(t)dt} = \int_0^\infty tE(t)dt \tag{2.2}$$

$$\sigma^2 = \int_0^\infty (t - t_m)E(t)dt \tag{2.3}$$

These two parameters are used to characterize the RTD and to calculate the dispersion coefficient. Assuming Danckwerts boundary conditions for an open-open system, the Peclet, Pe, (Bodestein, Bo) number, defined as the ratio of the rate of transport by convection to rate of transport by diffusion or dispersion, Pe = Ul/D, can be calculated from the following correlation

$$\frac{\sigma^2}{\tau^2} = \frac{2}{Pe} - \frac{3}{Pe^2} \tag{2.4}$$

Table 2: Results of RTD analysis, with calculated Peclet (Dispersion) values

	t_m (s)	Variance (s^2)	Pe	1/Pe	Flow rate (ml/min)	Fluid velocity (m/s)	Effective Diffusivity (m^2/s)
Single channel	8.4	40.348	5.881	0.17	8	0.021	0.00054
5x5co-12	23.219	507.157	4.167	0.24	2.5	0.00667	0.000238
5x5co-13	17.3377	426.259	3.183	0.314	2.31	0.006154	0.000288
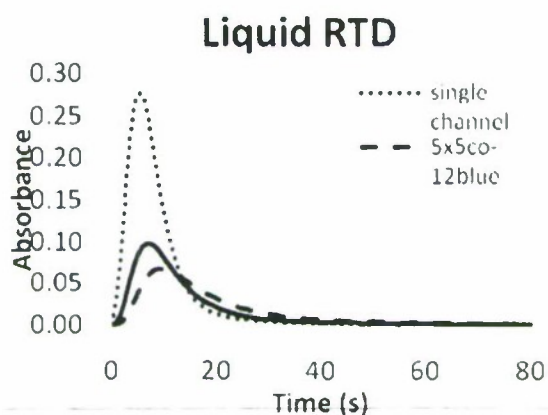
Liquid RTD

Figure 9: Liquid RTD Response for single-channel reference case and for 12- and 13-channels in cocurrent feed configuration in 5x5 distributor

From Figure 9, it can be seen that there is some dispersion attributed to the 5x5 distribution prototype being tested that causes the dye solution pulse to broaden as it moves down the channels. The Absorbance-time curve for the 5x5 distributor has a long tail and this causes a large spread, therefore large variance that contributes to very different Pe numbers (see Table 2) compared to the RTD through a single channel. As shown in **Error! Reference source not found.**, values for 1/Pe for all three experiments are in the range of 0.1 - 1, indicating that mild dispersive effects should be expected in the experimental system. In all three cases, RTD responses follow theoretical shapes commiserate with diffusive/dispersive mixing, and not from flow maldistribution (which is expected to produce multiple peaks, each corresponding to a unique flow path). *Thus, the present analysis indicates that the distributor prototypes are capable of uniform distribution, with mild contributions to dispersive mixing due to additional flow lengths.*

### 4.2.2.1. Residence Time Distribution. Gas-Phase Flow

Similar procedure as above was performed to calculate the Residence Time Distribution Function for the gas phase. The residence time distribution was determined experimentally by gas injections of Argon into the reactor under steady-state Helium flow. Argon partial pressure was measured in the effluent stream as a function of time using a Mass Spectrometer. The pressure vs. time profiles were obtained for: i) Flow through a single cordierite channel, ii) 5x5 microchannel reactor with gas injection through 12 channels, iii) 5x5 microchannel reactor with gas injection through 13 channels.
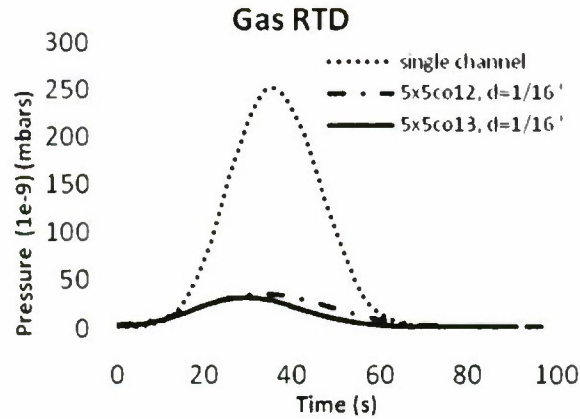
Figure 10: Gas RTD Response for single-channel reference case and for 12- and 13-channels in co-current feed configuration in 5x5 distributor

Additional measurements were performed in order to compare the RTD for a 5x5 microchannel network assembled with a top plate designed with channel diameter of 1/16" and a plate designed with channel diameter of 1/32" for additional pressure drop constriction.
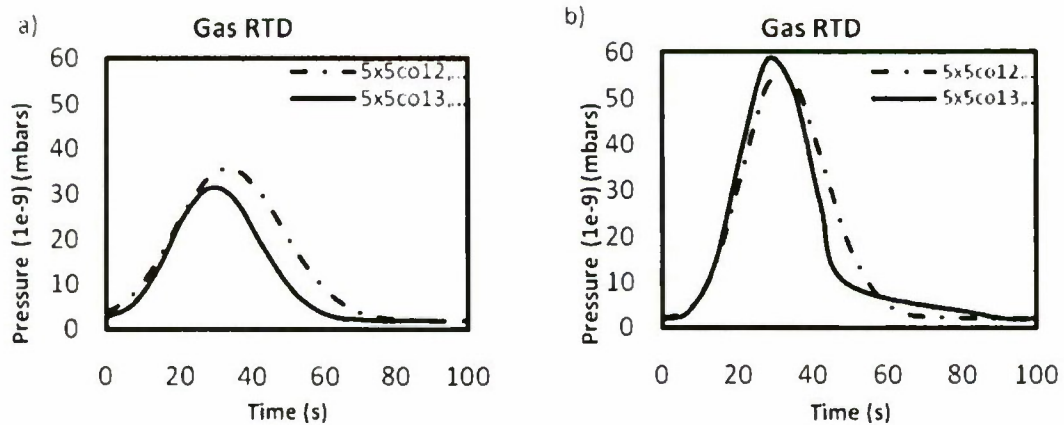
Figure 11: Gas RTD Response for a 5x5 acrylic distributor: a) top plate channel diameter=1/16", b) additional pressure drop constriction, top plate channel diameter=1/32"

Table 3: Results of gas residence-time distributor analysis, including calculated Peclet (Dispersion) values

	t_m (s)	Variance (s²)	Pe	1/Pe	Flow rate (ml/min)	Fluid velocity (m/s)	Effective Diffusivity (m²/s)
Single channel	36.3	103.721	28.936	0.0345	10	0.0267	0.000137
5x5co12-1/16"	38.17	421.09	9.757	0.102	10	0.0267	0.0273
5x5co13-1/16"	35.27	213.33	14.81	0.0675	10	0.0267	0.0180
5x5co12-1/32"	36.52	335.2	10.884	0.0919	10	0.0267	0.0245
5x5co13-1/32"	32.77	270.44	10.867	0.092	10	0.0267	0.0245

From the RTD results presented in Figure 10 and Figure 11 we could verify for all the cases studied, that there is some dispersion along the path of the gas, which may be attributed to laminarity of flow and diffusion. Since the RTD curve shows only one peak it can be concluded that the distributor does not present channeling and/or gas crossover within channels. The difference in areas and/or effective diffusivities can be attributed to the dilution factor used on the experiments. For the single channel reactor, 1 ml of Argon was injected in a stream of He/N$_2$ at a flow rate of 10 ml/min. For the 5x5 networks, 1 ml of Argon was injected in a stream of He/N$_2$ at a flow rate of 120 ml/min.

Additional experiments were performed after incorporating pressure drop constrictions at the distributor-monolith interface; these constrictions are 1/32" ID (as compared to the original 1/16" outlet ID), thus providing an identical limiting pressure-drop region for each flow path. This, in turn, is expected to provide greater flow uniformity across the distributor. Comparing the results obtained the 5x5 prototype with and without the pressure drop constriction, it can be verified that the top plate designed with smaller diameter (1/32") provides a better flow distribution. **Error! Reference source not found.** presents a summary of calculated dispersion coefficients obtained for gas-phase flows.

4.2.3. Heat Transfer Experiments in Mini-channel Systems

Initially the 3x3 acrylic prototype was used to verify model results for Case 1 (heat transfer between two non-reacting fluids). Cold water/hot water system was used to measure the heat transfer effectiveness (ε) and to monitor the temperature profile along the axial direction. Overall heat transfer effectiveness under non-reacting conditions was calculated by monitoring inlet and outlet temperatures for both hot and cold flows. Axial thermal profiles for counter-current flow

are obtained by embedding multiple thermocouples within the ceramic monolith wall. Data acquisition is automated through a PC equipped with Labview software.

In order to verify the model results for Case 1, multiple runs of different water flow rates were tested for counter-current configuration. The heat transfer effectiveness was calculated from Equation 7, based on the temperature data collected from inlet and outlet flows. From Figure 12, it can be seen that heat transfer effectiveness of about 20-40% were achieved for both cases. Increasing the water flow rate for both configurations consistently decreases the effectiveness. For instance, the effectiveness calculated at a flow rate of 8 ml/min corresponding to NTU=2.1 is of about 35%, increasing the flow rate to 15 ml/min for a NTU=1.4 decreases the effectiveness to 25%. Also, it is noticeable that the configuration "hot5cold4" (hot water flowing through 5 channels and cold water through 4 channels) is more thermally efficient than "hot4cold5" configuration.
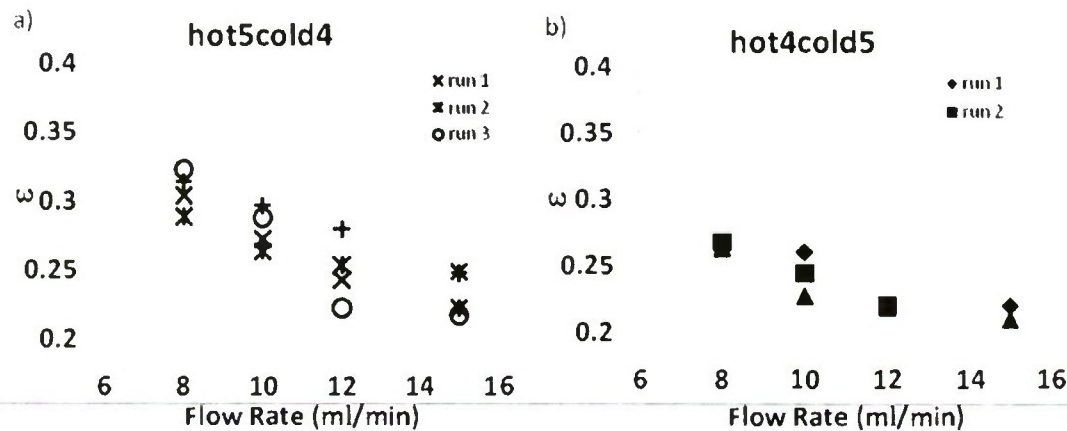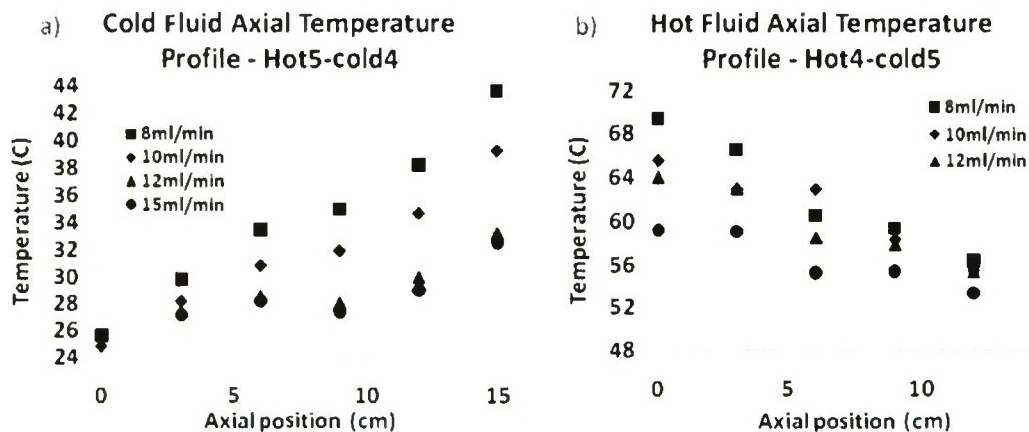

Figure 12: Heat transfer effectiveness for counter-current 3x3 microchannel network for a)hot water flow through 5 channels and b) hot water flow through 4 channels

Figure 13: Axial temperature profiles for a) Cold and b) Hot fluid flowing in 5-channel network (3x3 prototype).

Heat transfer experiments for cold/hot water system in the 5x5 checkerboard acrylic prototype were also performed to validate the model results of case I: Microscale Heat Exchanger. Effectiveness results from Figure 14 how that increasing the flow rate decreases the effectiveness as shown for the 3x3 prototype in Figure 12 (from 50% to 43%). Moreover, the 5x5 acrylic distributor prototype is certainly more efficient than the 3x3 network (effectiveness ~0.4-0.5 for 5x5 prototype vs ~0.2-0.3 for 3x3 prototype). This can be explained by the extra layer of channels that the 5x5 networks holds that adds more contact area, therefore more efficient heat transfer.

The addition of pressure drop constrictions by reducing the diameter of the distributor top plate from 1/16" to 1/32 not only does enhance the flow distribution as discussed on the previous section, it also improves the heat transfer in the device. Effectiveness results from Figure 14 confirms the last statement by showing an increase of about 10% with the decrease in channel diameter.
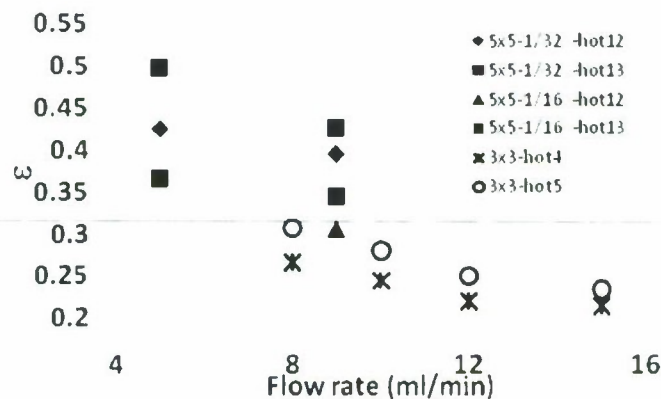
Figure 14: Effectiveness calculation for 3x3 and 5x5 acrylic prototypes

4.2.3. Comparison with Multi-Dimensional Models

In the modeling analysis, Case I: Microscale Heat Exchanger, the most important dimensionless parameters are the Number of Transfer Units (NTU) and the Conduction Parameter (CP), as defined by Equations 2.5-2.6. The parameter values are calculated from the experimental conditions for the hot-cold water system and using the appropriate thermal properties of both water and ceramic wall, as detailed in Table 4.

$$NTU = \frac{h_i a_i \tau_i}{\rho_i Cp_i}, \; CP = \frac{k_w}{\rho_i u_i Cp_i} \tag{2.5-2.6}$$

Table 4:Expected parameter values for Modeling Case I: Microscale Heat Exchanger

Design properties		Thermal properties		
diameter (m)	2.50E-03	$\rho(kg/m^3)$	1000	
length (m)	0.15	Cp (J/kgK)	4187	
surface area (m^2)	1.50E-03	μ(Pa.s)	0.0010	
area	6.25E-06	k(w/mk)	0.58	
volume (m^3)	9.375E-07	k_w (w/mK)	2	
a (area/volume)	1600.00	Prandlt(20°C)	7.01	
flow rate(ml/min)	5	10	15	
velocity (m/s)	0.0133	0.0267	0.04	
τ((s)	11.25	5.63	3.75	
Reynolds	33.33	66.67	100	
h(w/m^2K)	678.9	855.38	979.2	
NTU	*2.91*	*1.83*	*1.4*	
CP	*3.58e-5*	*1.79e-5*	*1.19e-5*	

As shown in Table 4, the experimental values for the NTU are within the range studied in the model simulations. However, the experimental CP's are lower compared to the simulated values. To be able to present a straight comparison between experiments and model prediction, a low limit value for CP was used to obtain model predictions for both adiabatic and isothermal packaging conditions. This is due to highly stiff ODE system that is unstable under very low conduction parameter values.
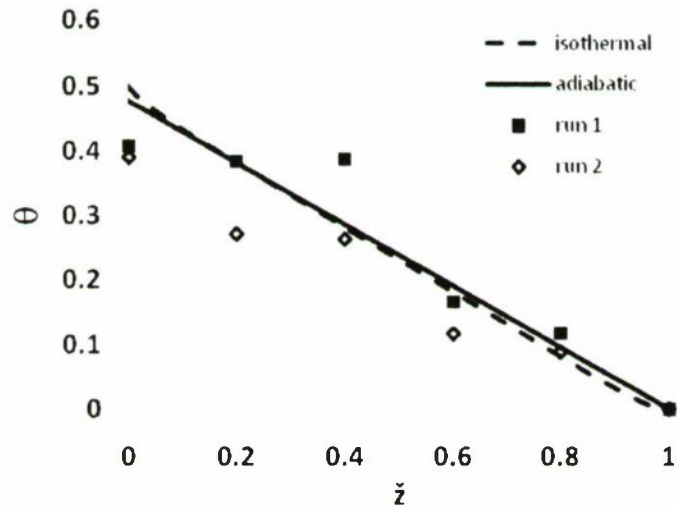
Figure 15:Hot/cold water system, flow rate = 10 ml/min. Model calculations for NTU=1.83 and CP<0.004

Simulated and experimental axial temperature profiles for the "cold flow" stream are presented in Figure 15. The results clearly show a substantial agreement between simulated model results for both adiabatic and isothermal packaging conditions and the experimental data for Case 1: Microscale Heat Exchanger. The model predicts $\varepsilon=0.476$ and $\varepsilon=0.498$ for the ideal cases of adiabatic and isothermal conditions respectively compared to the experimental value of $\varepsilon=0.4$.

4.5.2.4. Summary

Comparison of modeling results with experimental data for the case of heat transfer between two non-reacting fluids was performed using aqueous solutions in low-temperature acrylic prototypes. *Experimental results agreed with model predictions of thermal efficiencies ranging from 40 – 50%. Comparison of fluid thermal profiles with model predictions indicates good agreement between theory and the prototype system.*

4.3. Objectives for Period Three (10/01/08-05/31/10):

- Re-design distributors, refine fabrication plan
- Washcoat reforming catalyst
- Integrated reforming experiments
- Construct mems (silicon distributors)

4.3. Brass-Based Distributors for Microchannels

4.3.1. Construction of Intermediate-Prototype Brass Distributor

Three intermediate brass distributor prototypes were produced for the purpose of verifying high-temperature packaging methods, catalyst introduction and obtaining preliminary data ahead of Si-MEMS construction of final distributors. The distributor designs were based upon the original nine-channel checkerboard two-fluid distributor discussed in the original project proposal.

4.3.1.1. Investigation of High-Temperature Ceramic Sealants

Multiple high-temperature ceramic sealants were investigated for irreversible packaging of the twenty five -channel cordierite mini-channel network to the brass distributors. A graded adhesive joint was used to bond the cordierite monolith to the brass plates due to gross difference in Coefficient of Thermal Expansion (CTE) (Brass CTE ~19×10^{-6} 1/°C, cordierite's CTE ~0.5-0.6×10^{-6} 1/°C)). First each substrate was coated with the adhesive that best matched its CTE. A layer of *Aremco-Bond 598-A* (CTE 11.7×10^{-6} 1/°C) was applied to the brass plates; likewise the cordierite monolith was coated with *Ceramabond 618N* (CTE 0.59×10^{-6} 1/°C). Then, a third adhesive with an intermediate CTE *(Pyro duct 598-A* CTE 11.7×10^{-6} 1/°C) was used to bond the parts together. After numerous trials, it was discovered that the adhesives chosen were porous and did not have the consistency required for the brass plate and the ceramic monolith to successfully bond. The final mixture was grainy with large particulates, thus inappropriate for providing a precision seal within the tight machine tolerances of the distributor plate.

After this first attempt, ceramic, fiber, alumina and metallic based-type adhesives from Cotronics were evaluated: *901 Fiber based Alumina, 989 Alumina Ceramic, 950 Durabond Metallic Adhesive, 907 GF Resbond Adhesive and Sealing Putty.* The lack of success with any of the adhesives was attributed to the lack of surface contact between the monolith and the brass plate, material cracking after exposing the bonded material to high temperatures, glue consistency degraded/weaken when in contact with water and ultimately the monolith would break away from the brass plate. Based upon these results, distributor design was altered to enable the use of reversible compression-gasket seals.

### 4.3.1.2. Investigation of Graphite Compression Gaskets

After exploring a wide variety of high temperature sealants for irreversible packaging of the cordierite network to the brass distributors and experiencing the issues explained above, a

modified brass distributor relying upon a flat, machined graphite compression gasket with thickness of 1/16" for realizing leak-free and reversible sealing of mini-channel network to distributors was built.

The microreactor is comprised of two brass distributors, sealed to either end of the extruded ceramic microchannel network via compression chuck. Distributors were assembled from individually machined brass plates, and subsequently laminated to form the completed distributor, capable of directly addressing each microchannel with either a combustion (methanol, oxygen) and reforming (methanol, steam) mixture.

For this study three intuitive distribution distributors are identified in order to investigate the influence of radial distribution upon thermal integration and self-insulation for the case of hydrogen production from methanol via endothermic steam reforming coupled with exothermic methanol oxidation. Figure 16 presents cross-section illustrations of each integration scheme employed in the present study; the designs are as follows:

- Distributor A: checkerboard pattern coupling two separate volumes (combustion, steam reforming) while maintaining uniform radial temperature.
- Distributor B: annular pattern coupling two separate volumes (combustion, steam reforming) while providing radial self-insulation.
- Distributor C: annular pattern coupling three separate volumes (combustion, steam reforming, insulation) while providing radial self-insulation. For the present study, this third volume is kept empty in order to focus the study upon the potential for additional radial self-insulation in the absence of flow-folding (e.g., effluent cool-down, pre-heating) benefits.
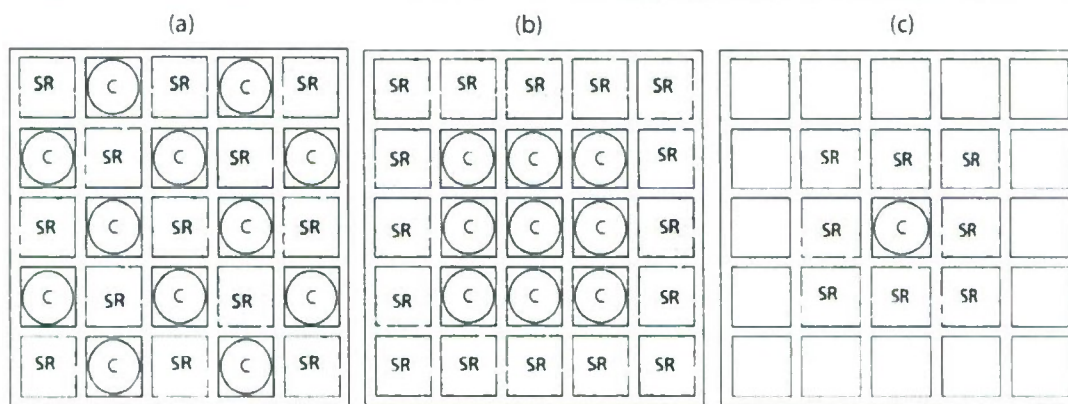
Figure 16: Cross-section illustrations for (a) Distributor A: Checkerboard pattern for coupling two separate volumes, (b) Distributor B: Annular pattern for coupling two separate volumes and (c) Distributor C: Annular pattern for coupling three separate volumes

4.3.1.3. Verification of Catalytic Washcoating Methods

Three distinct 5x5 microchannel networks for coupling methanol combustion and steam reforming were prepared in accordance with each of the three distributor distributors shown in Figure 16. For distributor A (Figure 16a), 12 channels were individually washcoated with combustion catalyst and the remaining 13 ehannels packed with reforming eatalyst. For distributor B (Figure 16b), 9 channels were washcoated with combustion catalyst and the remaining 16 channels packed with reforming catalyst. For distributor C (Figure 16c), a single channel was washcoated with combustion catalyst, 8 channels were packed with reforming catalyst, and the remainder were left empty. In all cases, dense fired cordierite honeycomb-monoliths with a cell density of 72 cells per square inch (CPSI) were supplied from Rauschert and used for eonstruction of microchannel networks. Preliminary results showed these substrates were found to have a slight porosity which resulted in a subtle flow crossover between reforming and eombustion channels. In order to minimize crossover, cordierite substrates were initially dip-coated with a nanopowder alumina layer as follows: Nanopowder alumina slurry was prepared by mixing nano-sized γ-alumina powder (Sigma–Aldrich), eolloidal alumina dispersion (20 wt%, Aldrich), distilled water and methanol (J.T. Baker) in the ratio of 1:0.5:10.5:10.5 by mass (Kim et al., 2009). Cordierite monolith was dipped into the slurry and then ultra sonicated at room temperature for 1 hour. This procedure was repeated three times while allowing sample to dry at room temperature for 1 hour between sonication steps. Coated sample was then calcined at 650°C for 4 hours with a heating and cooling rate of 5°C/min. This pre-treatment was found to remove any measureable flow crossover. Combustion catalyst (1 wt% Pt/Al$_2$O$_3$ powder from Sigma-Aldrich) washcoating solution was prepared in identical fashion to that detailed previously (Moreno and Wilhite, 2010). Blocking gaskets allowed selective coating of combustion channels only during dip-coating; monoliths were partially submerged in washeoating solution for approximately one minute, or until slurry level reached the mid-point of the microehannel length. Exeess solution was removed by pressurized gas, and the resulting system ealeined at 450°C for 4hr (heating rate 3°C/min and eooling rate of 3°C/min). This coating strategy guarantees that half of the combustion channel length is free of catalyst. Resulting catalytic coatings of thicknesses 200 – 300 μm were verified by scanning electron microscopy (SEM) analysis to be uniform and crack-free. (See Figure 17)

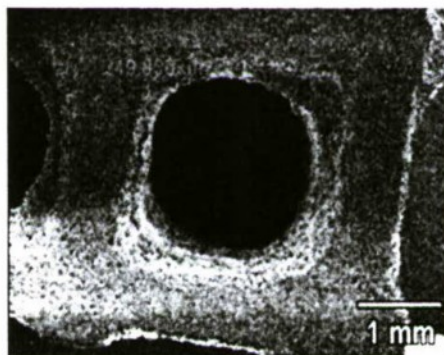**Figure 17: SEM images of 1 wt% Pt/Al$_2$O$_3$ catalyst deposited monolith**

4.3.1.4. Verification of Catalytic Packing Methods

For steam reforming, ceramic microchannels were packed with commercial catalyst based upon $CuO/ZnO/Al_2O_3$ formulation (Puristar R315 from BASF). Original catalyst is in the form of 5 mm pellets. These pellets were crushed and sieved between 500mm and 700mm (25-35 mesh), and sieved particles packed by hand into individual channels. Nickel mesh (100μ) (Alfa Aesar #44128) was inserted into reformer inlets and outlets to act as retaining screens. Each channel contained approximately 600 mg of catalyst.
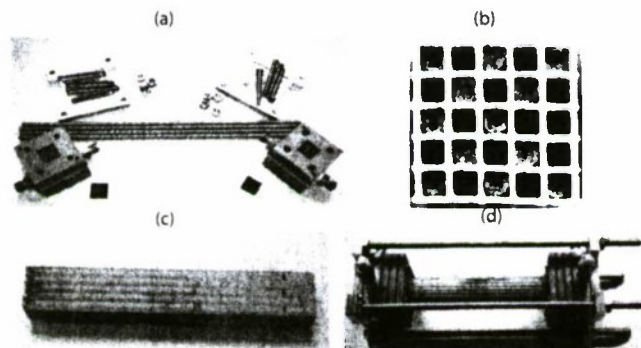
4.3.1.5. Distributor Construction

Brass plates were selected for the construction of each distributor, owing to suitable operating temperatures and ease of machining using in-house facilities. Four 2" x 2" brass plates were machined with two-dimensional patterns on either side, according to Figure 18. The three top-most plates were of thickness 1/8", to minimize size and weight; the bottom-most plate was 1" thick in order to accommodate conventional 1/16" nominal pipe thread (NPT) fittings for fluidic connections to the experimental apparatus. All prototype features and fluidic connections were 1/16", with the notable exception of 1/32" holes used on the top-most plate (at the distributor-ceramic microchannel interface). These uniform pressure restrictions act to compensate for any variations in pressure drop associated with individual flow paths; this strategy has been previously employed in microchemical systems with complex distribution networks to ensure uniform flow distribution (Amador et al., 2004;Wada et al., 2006). Final distributor assembly was accomplished by compression sealing the four-plate stack with silicon gaskets between each plate. Silicone rubber gaskets (McMaster-Carr) were also used for compression sealing either face of the ceramic microchannel network to brass distributors.

4.3.1.6. Microreactor Assembly

The microchannel network was assembled by metal plates attached to each brass distributor block. One end (metal plate/brass distributor block) is fixed and the other end is compression sealed to extruded ceramic microchannel network by adjustable screws. Silicone gaskets (1/16") were placed in the recessed face of each distributor, followed by either end of the ceramic network. This set-up allows leak-free and reversible sealing of microchannel network to distributors. (See Figure 19)
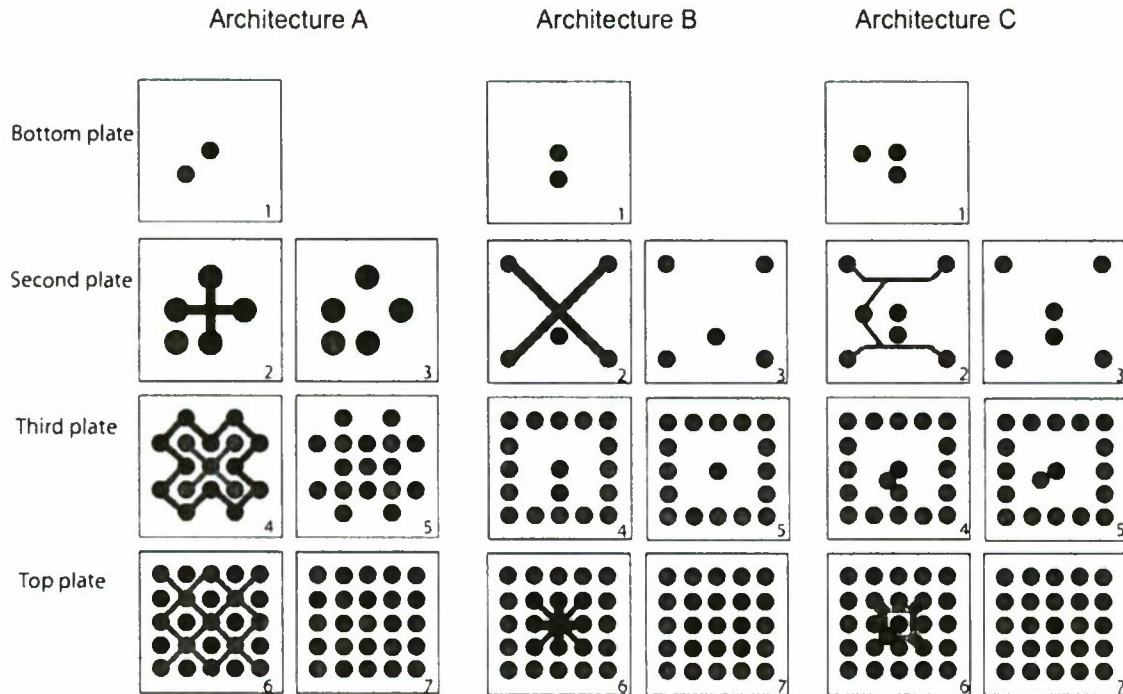
Figure 18: Schematic of distributor layers for 2-D complex distribution schemes: 1. Bottom plate: Fluid A and fluid B main inlets; 2. Second plate-bottom: fluid A undergoes first level bifurcation; 3. Second plate-top: End of first bifurcation; 4. Third plate: End of second bifurcation level; 6. Top plate-bottom: Second level bifurcation of fluid B, 7. Top-top: End of third bifurcation level

Figure 19: Construction of the 5x5 microchannel network; (a) distributors, (b) Cross-section of microchannel network, (c) side-view of microchannel network,(d) final assembly with four-point compression chuck.

4.3.2. Microreactor Operation

Once assembled, each of the three microreactors were investigated over a range of combustion and/or reforming flow rates while varying the oxygen content of the combustion feed. Methanol vapor and oxygen was supplied to combustion channels by blending 20% O_2/5%He in Ar with ultra-high purity Ar and passing through an isothermal bubbler containing 99.9% purity methanol (J.T. Baker). An equimolar mixture of distilled water and methanol was supplied to the reforming channels by passing a dry 5% N_2/Ar mixture through a second bubbler containing 115 mL and 285 mL of methanol and distilled water, respectively. Both bubblers, thermostated by a heating tapes attached to temperature controllers were kept at 20°C such that feed molar fraction of methanol was maintained at 13% and 2% in combustion and reforming inlet streams, respectively. Gas flow rates were controlled using Alicat Scientific digital flow controllers. Dry gasses were supplied by Airgas.

Analysis of reaction products was provided on a dry-gas basis by an Agilent MS3000 gas chromatograph, employing Ar carrier gas, such that N_2 and He served as internal standards for computing effluent flow rates for reforming and combustion channels, respectively. Two condensers maintained at 273K and 195K were placed in series between gas effluent and the gas chromatograph in order to remove all moisture and unreacted methanol.

Combustion inlet oxygen/methanol molar stoichiometric ratio, defined as the equivalency ratio (ER), was varied from 0.5 to 1.0 (Equation 3.1) in the present study. Methanol conversion in both reforming and combustion channels was calculated from the output molar flow rate of methane, carbon monoxide and carbon dioxide (Equation 3.2). Product yields reported below were calculated based on the theoretical maximum for each product (Equation 3).

$$ER = \frac{F_{O_2}}{1.5 \cdot F_{CH_3OH}} \tag{3.1}$$

$$X_{CH_3OH} = \frac{F_{CO} + F_{CH_4} + F_{CO_2}}{F_{CH_3OH,inlet}} \tag{3.2}$$

$$Y_{CO} = \frac{F_{CO}}{F_{CH_3OH,inlet}}; Y_{CO_2} = \frac{F_{CO_2}}{F_{CH_3OH,inlet}}; Y_{CH_4} = \frac{F_{CH_4}}{F_{CH_3OH,inlet}};$$

$$Y_{H_2,comb} = \frac{F_{H_2}}{2 \cdot F_{CH_3OH,inlet}}; \ Y_{H_2,ref} = Y_{H_2,overall} = \frac{F_{H_2}}{3 \cdot F_{CH_3OH,inlet}} \tag{3.3}$$

4.3.3. Results and Discussion

4.3.3.1 Distributor A: Radially Uniform Integration of Two Volumes

The first distributor distributor allocates a steam reforming flow amongst 13 channels and a separate combustion stream amongst the remaining 12 channels to achieve a thermally uniform

and balanced integration of the two processes. Combustion channel flow rate (Re_{comb}) and composition (ER) was varied to identify optimum operating conditions. Combustion equivalence ratio (ER) was varied from 0.5 to 1.0 for three different combustion Reynolds' numbers of 150, 200 and 250 corresponding to total flow rates of 900, 1200 and 1500 sccm. Reforming channel flow rates were maintained at a Reynolds' number of 250, corresponding to a total flow rate of 1600 sccm for all conditions studied. Methanol mole fraction was maintained at 13% in combustion channels, and 2% in reforming channels for all conditions studied.

The combustion reaction was first ignited with stoichiometric O_2/CH_3OH ratio (ER=1). After ignition, the steam reforming flow was started. Once the flame stabilized, the fuel composition was reduced from ER=1 to 0.5 at intervals of 0.1 while maintaining a constant flow rate. Same procedure is used for all three prototypes at the flow rates analyzed.

Selectively coating half of the combustion channel length with catalyst places fuel ignition at the axial mid-point; however, combustion flow rate and composition as well as reforming flow direction are found to have substantial influence upon final hot-spot location. Co-current operation resulted in a stable hot-spot location near the microchannel outlet, while counter-current operation resulted in a hot-spot location at the axial mid-point; this is attributed to additional combustion heat dispersion provided via the reforming stream. Thus, all experiments for distributors A, B and C were performed in counter-current flow.

Hot-spot magnitude

Hot-spot magnitude as a function of ER and Re_{comb} is presented in Figure 20. At ER = 1, hot-spot was located at the axial mid-point corresponding to the point at which fuel and oxidant first contact the combustion catalyst. Under these conditions, the hot-spot has a symmetrical shape with a maximum temperature of 560^0C while both distributors remained at ~ 50°C. As ER is reduced, hot-spot position does not shift; however the maximum temperature decreases to a minimum of 260°C corresponding to an ER = 0.5 and Re_{comb} = 150. Further reductions in ER resulted in hot-spot extinction, regardless of combustion flow rates.

Extent of Reaction

The influence of combustion flow rate (Re_{comb}) and equivalence ratio (ER) upon methanol conversion is summarized in Figure 21a-c. Methanol conversion in the steam reforming channels remained constant at Re_{ref} = 250 over the range of combustion equivalence ratios (ER) studied. Reduction in methanol supply to the combustion volume (via Re_{comb}) resulted in decreased methanol conversion in the reforming channels owing to reduced system temperature, with this effect becoming more pronounced at ER < 0.7. Figure 21b shows the effect of ER and Re_{comb} on the performance of the microchannel combustor. As ER was reduced from 1 to 0.5, methanol conversions in the combustion channels decreased from 98% to 42%. In addition, methanol conversion decreased mildly with increasing flow rate, owing to a reduction in the residence time. Overall methanol conversion (Figure 21c) reflects a combination of these two trends such that total methanol conversion decreases with combustion ER regardless of Re_{comb}
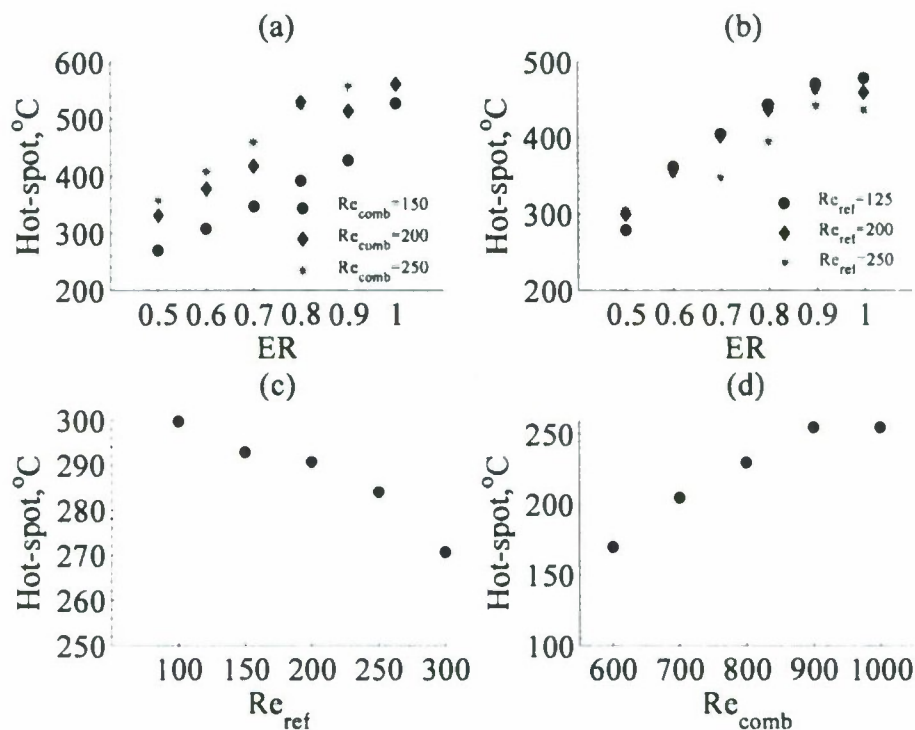
Figure 20: Effect of Re$_{comb}$ and ER upon hot-spot magnitude in distributor A

. Carbon Monoxide Formation

The influence of both Re$_{comb}$ and ER upon carbon monoxide formation is summarized in Figure 21g-i. As the hot-spot magnitude increases through increasing ER from 0.5 to 1.0, carbon monoxide yields increase from 10% to 30%. This is attributed to a change in the water-gas-shift equilibrium to the reactant side as excess combustion heat accumulates within the reforming volume, thus favoring carbon monoxide formation. In the combustion channels, a maximum carbon monoxide yield of 32% was observed at ER = 0.8 and Re$_{comb}$ = 250. Further increases in ER reduced carbon monoxide yield as selectivity shifted towards carbon dioxide formation. The overall carbon monoxide yield trends are dominated by those of the combustion channels, owing to the relatively large amount of fuel supplied to the combustion volume.

Methane formation

The effect of both Re and ER in the combustion channels on methane formation is summarized in Figure 21j-l. In the reforming channels, the molar concentration of methane was almost always below detection limits, while combustion channels achieved <3% methane yield under all conditions.
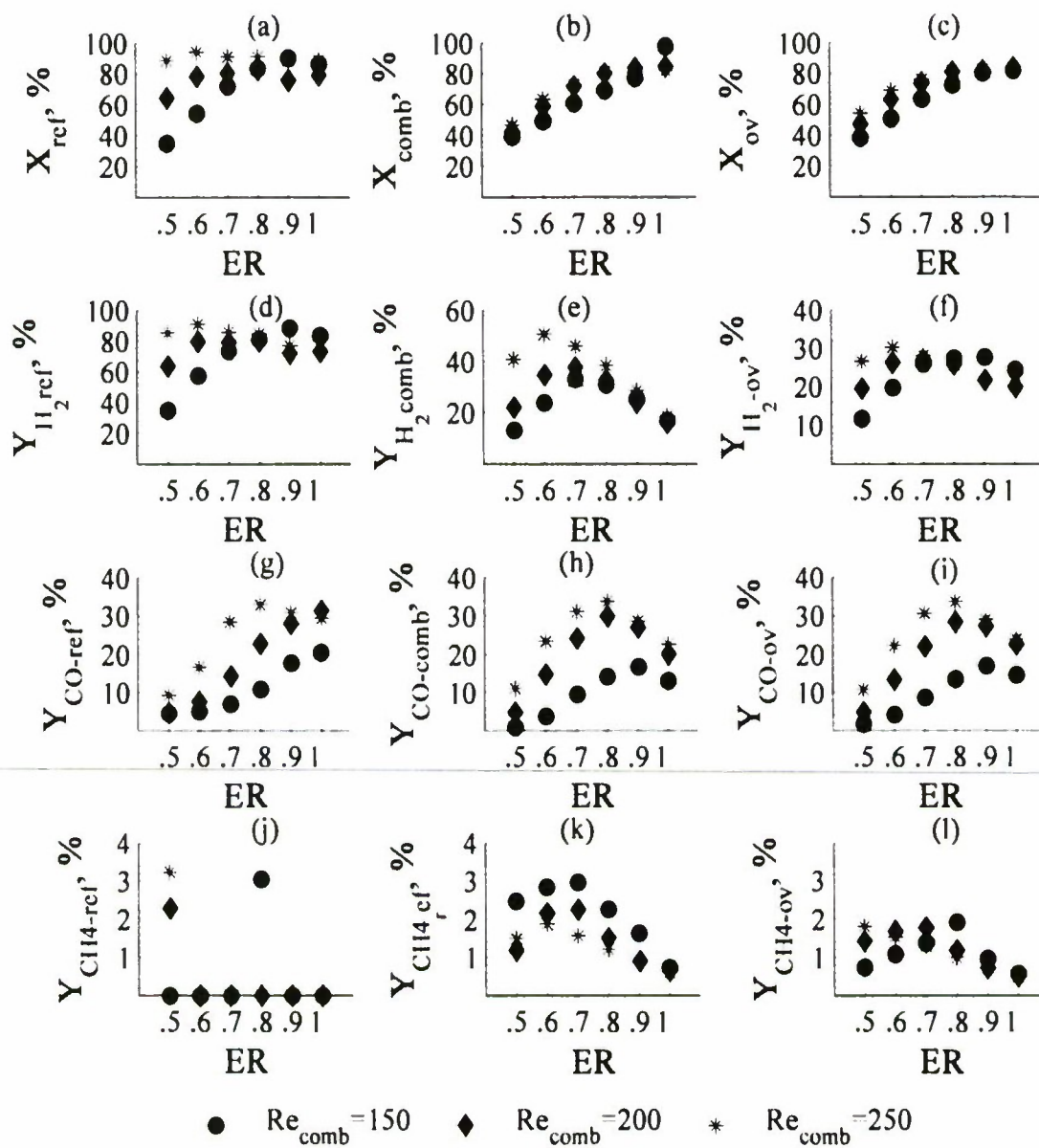
Figure 21: Distributor A: Effect of ER and Re in combustion channels on (a-c) Methanol conversion, (d-f) Hydrogen yield, (g-i) Carbon monoxide formation, (j-l) methane formation

Hydrogen Production

Figure 21d-f indicates that an ER of $0.5 - 0.6$ is necessary to achieve both high hydrogen and low carbon monoxide yields. At $Re_{comb} = 250$ and $ER = 1$, the hot-spot temperature is $560°C$, which is sufficient to achieve hydrogen yields in excess of 90% in the reforming volume. As ER is reduced the hot-spot temperature decreases from $560°C$ to about $300°C$ at $ER = 0.5$ and $Re_{comb} = 250$, which favors the production of carbon dioxide (Figure 21g). Reduction in equivalence ratio (ER) also favors hydrogen production via partial oxidation in the combustion volume, as shown in Figure 21e; a maximum in combustion volume hydrogen yield of 51% was obtained for an $ER = 0.6$ at $Re_{comb} = 250$.

The maximum hydrogen yield for the autothermal reformer reflects a combination of both steam reforming and partial oxidation (combustion volume) performance. As Re_{comb} is increased, the maximum overall hydrogen yield shifts to lower equivalency ratios, reflecting the importance of hydrogen yields from the combustion volume which consumes a substantial amount of methanol fuel. At $Re_{comb} = 150$, maximum hydrogen yield of 28% was observed at an $ER = 0.9$; at $Re_{comb} = 200$, the maximum yield corresponded to $ER = 0.7$; at $Re_{comb} = 150$, maximum hydrogen yield of 30.3% was observed at $ER = 0.6$. These results indicate that maximum hydrogen yields correspond to operation of the heat-exchanger microreactor as a combination of partial oxidation and steam reforming.

4.3.3.2. Distributor B: Annular Integration of Two Volumes

The second distributor allocates a steam reforming flow amongst 16 channels and a separate combustion stream amongst the remaining 9 channels in a radial distribution pattern approximating a conventional shell-and-tube heat exchanger. The system performance was investigated for combustion equivalence ratios (ER) of 0.5 to 1 and reforming flow rates of 1000, 1600 and 2000 sccm, corresponding to individual-channel reforming Reynolds' numbers of 125, 200 and 250, respectively. Combustion flow rates were maintained at 1125 sccm, corresponding to a Reynolds' number of 250. This value was selected based upon best performances observed with distributor A.

Hot-spot Magnitude

The effect of combustion ER on hot-spot magnitude for all three reforming flow rates is summarized in Figure 20. The hot-spot was located at the axial mid-point of the reactor and spanned the majority of the microchannel network with a maximum external temperature of $430°C$. As ER is reduced, the hot-spot magnitude decreased to $300°C$ at $ER = 0.5$, with distributor temperatures remaining at $40 - 50°C$ for all conditions. Furthermore, increasing Re_{ref} decreased hot-spot magnitude, owing to a combination of greater heat removal and utilization by the reforming stream.

Extent of Reaction

The influence of reforming flow rate and combustion equivalence ratio (ER) upon methanol conversion is summarized in Figure 22a-c. Methanol conversion in the steam reforming channels remained > 90% over the span of ER values investigated when operated at the lowest reforming flow rate (Re_{ref} = 125). For the case of Re_{ref} = 200, methanol conversions drop to 60% as ER is reduced to 0.5; similarly at Re_{ref} = 250 conversions reduce to 10% at ER = 0.5. This data suggests that a combination of insufficient partial oxidation/combustion heat and decreased reforming residence times significantly limit methanol conversion. This behavior is similar to that observed in Distributor A when hot-spot magnitude was decreased by lowering combustion flow rates, suggesting that thermal effects dominate residence-time effects. Likewise, the influence of ER on methanol conversion in combustion channels is identical to that observed for distributor A, and can again be attributed to a lack of sufficient oxidant at low ER values.

Carbon Monoxide Formation

The influence of both Re_{ref} and ER upon CO formation is summarized in Figure 22g-i. As hot-spot magnitude increases (via decreasing Re_{ref}), both reforming and combustion carbon monoxide yields increase. This can be attributed to the accumulation of excess reaction heat shifting chemical equilibrium in favor of carbon monoxide production. Increasing ER from 0.5 resulted in an initial increase in carbon monoxide formation owing to this effect; as ER is increased beyond 0.8, carbon monoxide yields decrease owing to combustion stoichiometry favoring complete combustion.

Methane Formation

The results for methane formation at the conditions studied are shown in Figure 22j-l. As was the case for Distributor A, reformate methane yields were below the gas chromatograph's detection limit. Low (<1%) combustion methane yields were observed over the full range of Re_{ref} and ER studied.

Hydrogen Production

The effect of Re_{ref} and ER upon hydrogen yield is summarized in Figure 22d-f. At low flow rates (Re_{ref} = 125), reforming hydrogen yield was not strongly influenced by decreasing ER, instead remaining at ~ 80%. As noted above, reducing the combustion ER at high reforming flow rates (Re_{ref} = 250) significantly reduced hot-spot magnitude and thus methanol reforming rates and hydrogen yields. Increasing reforming flow rate strongly influenced hydrogen yields in the combustion channels. While a maximum hydrogen yield of 33% was measured at low reforming flows (Re_{ref} = 125), less than 10% hydrogen yields were observed when reforming flow rate was doubled (Re_{ref} = 250). Further increases in Re_{ref} resulted in reduced methanol conversion in the combustion channels, thus low hydrogen yields, and a highly unstable behavior prone to quenching at low ER values.
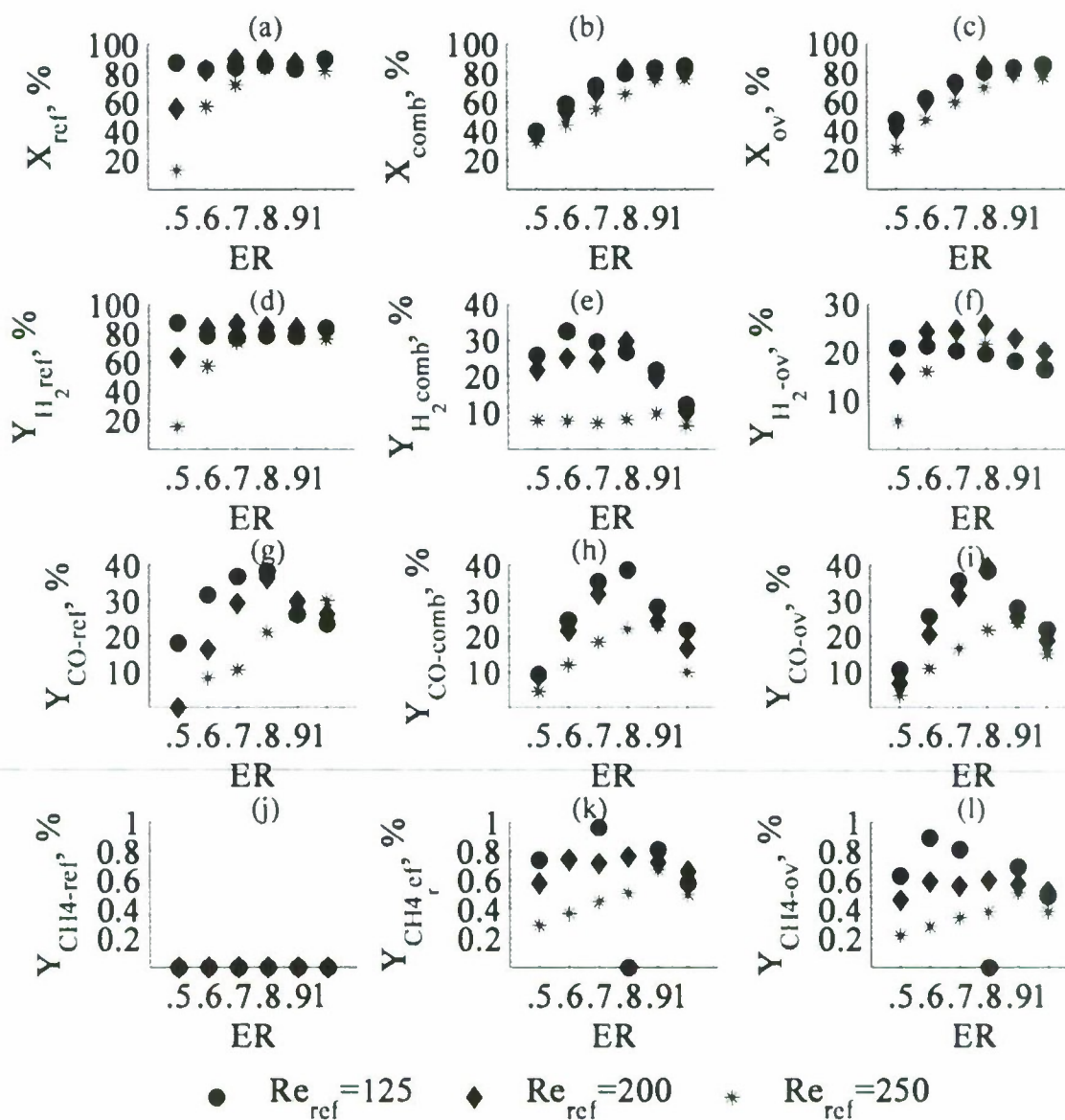
Figure 22: Distributor B : Effect of ER and Re in reforming channels on (a-c) Methanol conversion, (d-f) Hydrogen yield, (g-i) Carbon monoxide formation, (j-l) Methane formation

A maximum overall hydrogen yield of 26% was observed at Re_{ref} = 200 and ER = 0.8; under these conditions both endothermic reforming and exothermic partial oxidation volumes were producing hydrogen. Combustion/partial oxidation hydrogen yields were lower than those observed under similar conditions (Re_{comb} = 250, ER = 0.7) while carbon monoxide yields were slightly higher, suggesting that the annular-layered distribution design did result in higher internal temperatures corresponding to the exothermic combustion channels. However, heat losses to ambient from the outer layer of steam reforming channels limited overall hydrogen yields via necessitating relatively high combustion flow rates.

### 4.3.3.3. Distributor C: Annual core distribution pattern

The final distributor investigated in the present work allocates combustion flow to a single, central channel; steam reforming flow is allocated in the 8 channels adjacent to the combustion channel, while a third heat utilization / retention volume is allocated to the outermost 16 channels. For the present analysis, this third volume is scaled in order to provide heat retention while enabling a direct comparison between all three distributors for the coupling of steam reforming and combustion. Findings provide a basis for indentifying appropriate functions for this third volume in subsequent studies, such as reactant pre-heating or vaporization, or effluent cool-down or hydrogen cleanup via water-gas-shift.

In reducing the combustion to reforming volume ratio from 3:4 to 1:8, conditions for stable high-temperature operation changed markedly between distributor B and C. Initial experiments varying the combustion ER indicated that an ER of unity was required to achieve results that were comparable to previous distributors. For this reason, performance was studied at combustion ER = 1 while varying combustion and reforming flow rates.

4.3.3.3.1 Influence of Varying Re_{ref} at fixed Re_{comb} = 1000

The influence of reforming flow rates upon combustion hot-spot magnitude and reformer performance was investigated at a constant combustion flow rate of 500 seem, corresponding to Re_{comb} = 1000. Reformer flow rates of 400, 600, 800, 1000 and 1200 seem were employed, corresponding to Rc_{ref} = 100, 150, 200, 250 and 300.

The effect of Re_{ref} upon hot-spot magnitude is shown in Figure 20. It is important to note that temperatures reported from thermal imaging correspond to the microchannel network's surface temperature, which was substantially lower than those reported for distributors A & B; this suggests that the additional heat retention channels in distributor C are contributing to the radial insulation of the microchannel network. The maximum hot-spot temperature observed was 300°C, corresponding to the lowest Re_{ref} investigated (Re_{ref} = 100). As Re_{ref} increased to 300, hot-spot magnitude decreased from 300°C to 270°C. Additionally, increases in Re_{ref} resulted in downstream shifting of the hot-spot location towards the reforming outlet / combustion inlet. This is attributed to increased combustion heat dispersion by the reforming stream. Figure 23a shows the effect of varying Re_{ref} upon methanol conversion. Methanol conversion decreased from 100% at Re_{ref} = 100 to 88% at Re_{ref} = 300, owing to reduced residence times. Rc_{ref} was also found to influence methanol conversion in the combustion volume; as Rc_{ref} was increased from 100 to 300, methanol conversion in the combustion volume decreased from 66% to 63%.
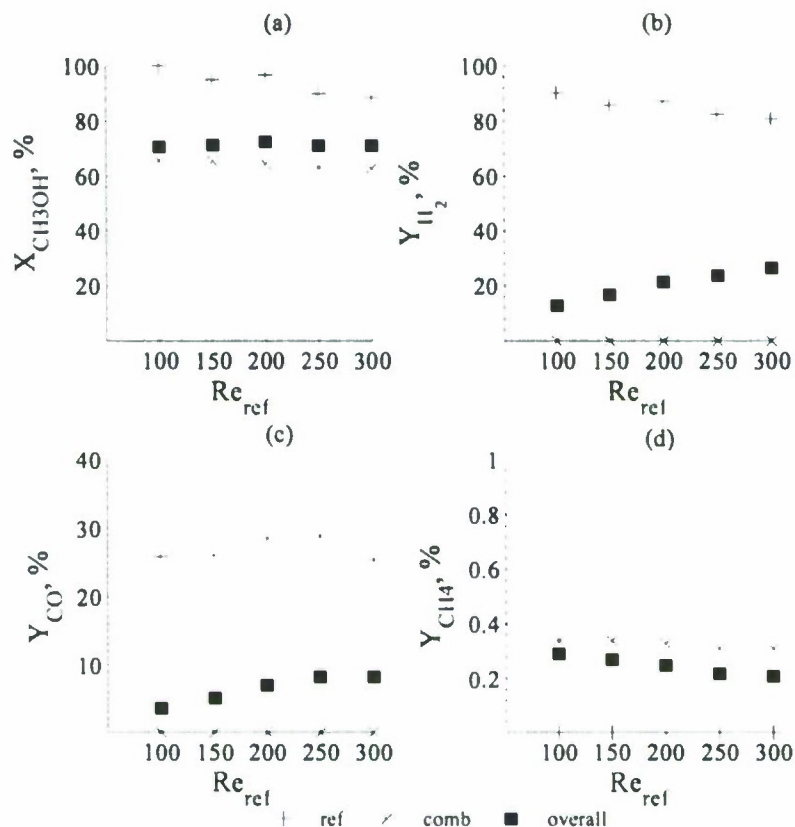
Figure 23: Distributor C: Effect of Re_{ref} on (a) Methanol conversion, (b) Hydrogen yield, (c) carbon monoxide formation and (d) methane formation

Steam reforming carbon monoxide yields remained relatively steady at ~ 27% for all Re_{ref}, as shown in Figure 23c, while an ER of unity in the combustion channels resulted in < 1% carbon monoxide yields under all Re_{ref} studied. Thus, overall carbon monoxide yields were observed to increase from 3% to 8% with increasing Re_{ref} from 100 to 300.

Figure 23d shows the influence of Re_{ref} upon methane formation. Methane yields of < 0.4% were observed in the combustion effluent for all Re_{ref}, corresponding to overall methane yields of < 0.3%.

The effect of Re_{ref} upon hydrogen yield is presented in Figure 23b. At Re_{ref} = 100, hydrogen yield in the reforming volume is 90%; this decreases to 81% at Re_{ref} = 300, owing to reduced methanol conversion in response to lower residence times. Unlike previous experiments with distributors A and B, hydrogen generation only occurred in the reforming volume; carbon dioxide, steam and trace amounts of methane were the sole products present in the combustion effluent.

4.3.3.3.2. Influence of Varying Re_{comb} at fixed Re_{ref} = 250

Combustion flow rates of 500, 450, 400, 350 and 300 sccm, corresponding to Re_{comb}=1000, 900, 800, 700 and 600, were employed to ascertain the extent to which combustion flow rate may be reduced without altering overall system performance and thus maximize hydrogen yields.

The influence of Re_{comb} upon hot-spot position and magnitude is shown in Figure 20. System temperature decreased from 250°C to 170°C as Re_{comb} decreased from 1000 to 600. As noted above, these maximum observed temperatures correspond to the outer surface temperature, which is expected to be lower than the internal reforming or combustion temperatures. For all conditions, axial heat conduction was sufficiently low that distributor blocks remained at temperatures < 50°C.

The effect of Re_{comb} on methanol conversion is shown in Figure 24a. Methanol conversion in both reforming and combustion channels decreased with Re_{comb}, due to reductions in reaction temperatures and thus reaction rates; further decreases in Re_{comb} below 600 resulted in unstable hot-spot leading to extinction.
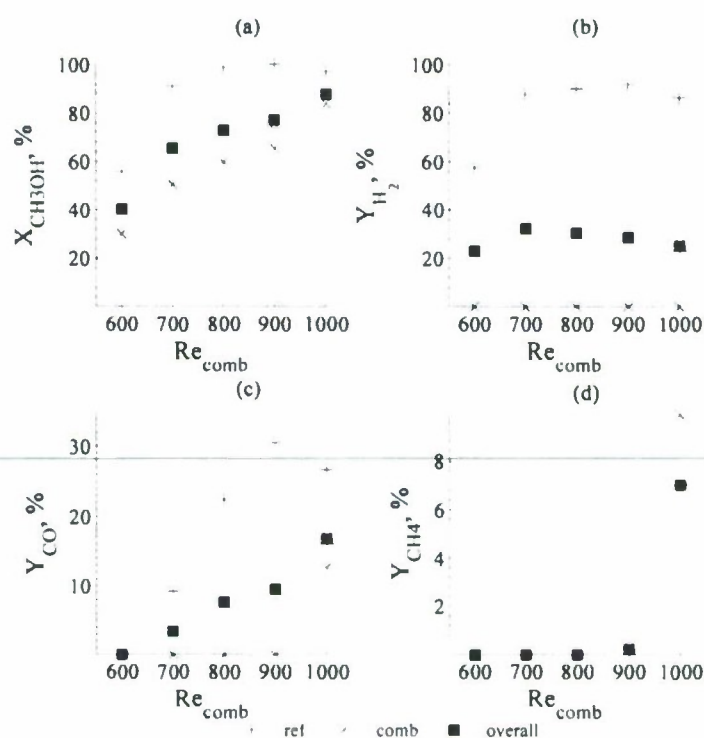
The effect of Re_{comb} upon carbon monoxide formation is shown in Figure 24c. It is interesting to note that while carbon monoxide yields of ~ 30% are observed at Re_{comb} < 900, very low carbon monoxide yields (< 10%) were observed at Rc_{comb} < 700. This indicates that the reduced hot-spot magnitude and width (shown in Figure 20) enabled additional water-gas-shifting to occur; it is hypothesized that the hot-spot provided a catalytic cool-down region in the reforming channels that enabled a rapid shifting of carbon monoxide produced in the high temperature hot-spot region. Current research efforts are aimed at investigating this unexpected benefit of the sharp axial thermal gradients achieved using this cordierite microchannel network.

Methane yields were negligible under all conditions except for Re_{comb} = 1000, which corresponded to 9% yield in the reforming channels at an observed hot-spot temperature of 250°C.

From Figure 24b, hydrogen yield in the reforming volume was shown to be strongly influenced by Re_{comb}, again owing to reduced reaction temperatures and therefore rates at combustion flow rates. While reformer hydrogen yields were stable and > 80% for all Re_{comb} > 700, further increases in combustion flow rate resulted in more fuel combustion and therefore lower overall hydrogen yields; additionally the higher reforming temperatures achieved at Re_{comb} > 900 resulted in increased carbon monoxide production. Thus, optimal performance for distributor C was observed at Rc_{comb} = 700, corresponding to an overall hydrogen yield of 32% and carbon monoxide yield of 4%. Under these conditions, the external hot-spot temperature was observed to be 200°C, with a methanol conversion of 90% and carbon monoxide yield of 10% in the reforming volume; data obtained for identical single-channel reforming flow rates using distributor B (Figure 22) at a combustion ER = 0.6 corresponded to an observed hot-spot external temperature of ~300°C. Likewise, at an identical single-channel reforming flow rate (Re_{ref} = 250) in distributor A, equivalent methanol conversions and carbon monoxide yields were observed at a combustion flow rate of Re_{comb} = 250 and ER = 0.5, which resulted in a hot-spot

external temperature of ~360°C. This comparison of hot-spot magnitude under identical reforming flow rates, conversions and yields strongly suggests that (i) the annular distribution scheme introduced in distributor B contributed to a reduction in reactor surface temperature of ~50°C, while (ii) the additional annular heat retention layer introduced in distributor C contributed to a further reduction in reactor surface temperature by ~ 100°C. This analysis confirms that the use of complex, two-dimensional radial distribution patterns are capable of creating three-dimensional thermal gradients which may be exploited to enhance hydrogen and/or carbon dioxide yields. However, in the absence of external insulation, maximum hydrogen yields were limited to ~30% for all three distributors.

Figure 24: Distributor C: Effect of Re_{comb} on (a) Methanol conversion, (b) Hydrogen yield, (c) carbon monoxide formation and (d) methane formation

4.3.4. Conclusions

Results demonstrate the influence of distribution patterns, individual process flow rates and therefore relative process enthalpies and contribution of heat dissipation upon resulting thermal gradients and reactor performance for the autothermal production of hydrogen from methanol. The three designs are as follows: Distributor A represents a checkerboard pattern coupling two separate volumes (combustion, steam reforming) while maintaining uniform radial temperature with a ~1:1 volume ratio of combustion to reforming; distributor B represents an annular pattern

with a 3:4 volume ratio of combustion to reforming while providing radial self-insulation, and distributor C couples three separate volumes: a single channel for combustion catalyst, 8 channels for reforming, while the outer sixteen channels serving as a heat retention volume, providing radial self-insulation.

In the absence of any external insulation, distributor A & B achieved highest hydrogen yields when operated as a combination of steam reforming and partial oxidation, owing to near-unity volume ratios; while distributor C achieved highest hydrogen yields when operated as a combination of combustion and steam reforming; owing to 1:8 volume ratio which approach the 11:1 ratio of reaction enthalpies. Thermal imaging analyses demonstrated that all three distributors are capable of axially isolating hot-spots during operation; this in turn enabled the use of relatively low-temperature reversible gasket sealing and construction materials for distributors, while greatly reducing heat losses to packaging. In addition, comparison of external hot-spot magnitude for all three distributors operating at identical single-channel reforming flow rates and similar reforming yields strongly suggests that radial distribution designs are capable of creating substantial (50 – 150°C) radial thermal gradients in the small (5x5) microchannel network. Hence results clearly demonstrate how distribution distributors allow manipulation of three-dimensional hot-spots. Even though findings demonstrate the value of axial self-insulation achieving net hydrogen yields of 20-32% for all three distributors, they also indicate that variations in radial distribution schemes were not able to limit radial heat losses to surroundings.

4.4. Fabrication of Silicon Distributors

Using conventional machining technology, three 5x5 (25-channel) prototypes fashioned out of brass material were constructed for the autothermal production of hydrogen from methanol. While we were able to demonstrate the proof of concept by using this technology, conventional machining presents restrictions on scaling up and fabrication of high-precision microscale structures with complex patterns as it is limited to sizes down to 1/32 in. As pattern complexity and size grows from 5x5 networks to larger systems (extrudates are available on sizes up to 10^4 channels, conventional machining becomes unreasonable. Si-MEMS technology was investigated for miniaturization (reduced weight and volume) of the 5x5 designs.

This section details the design, fabrication and demonstration of the first generation of microfabricated silicon distributors for packaging ceramic microchannel networks, in order to reduce overall system volume and weight. By using photolithography and chemical etching techniques employed by microelectromechanical (MEMS) and microchemical systems the three distributors detailed above for autothermal hydrogen production from methanol are built.

The fabrication strategy consists of four silicon wafers, containing a total of eight layers comprising the overall microfluidic network analogous to technique described in Chapters 3 and 4. Fusion bonding technique allows high-temperature, high-pressure sealing between individual plates (London et al., 2001; Mirza and Ayon, 1999) to complete the four-wafer stack. The resulting distributors will be compression-sealed to a 5x5 ceramic microchannel network for the heat integration of steam reforming and combustion of methanol for hydrogen production.

4.4.1. Distributor Designs

Distributor designs utilize silicon microfabrication methods to fabricate three complex two-dimensional distribution patterns across the microchannel network. Figure 25-27 present 3-D illustrations of each integration scheme employed in the present study; the designs are as follows:

- Distributor A: checkerboard pattern (Figure 25) coupling two separate volumes (combustion, steam reforming) while maintaining uniform radial temperature.
- Distributor B: annular pattern (Figure 26) coupling two separate volumes (combustion, steam reforming) while providing radial self-insulation.
- Distributor C: annular pattern (Figure 27) coupling three separate volumes (combustion, steam reforming, insulation) while providing radial self-insulation. For the present study, this third volume is kept empty in order to focus the study upon the potential for additional radial self-insulation in the absence of flow-folding (e.g., effluent cool-down, pre-heating) benefits.
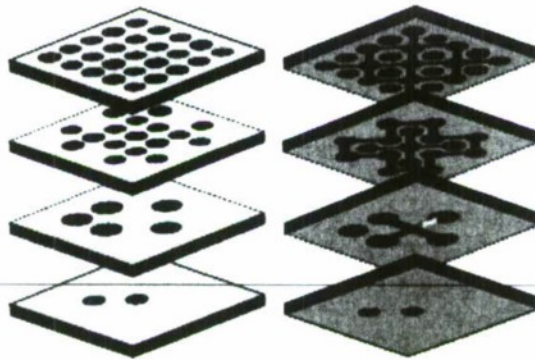

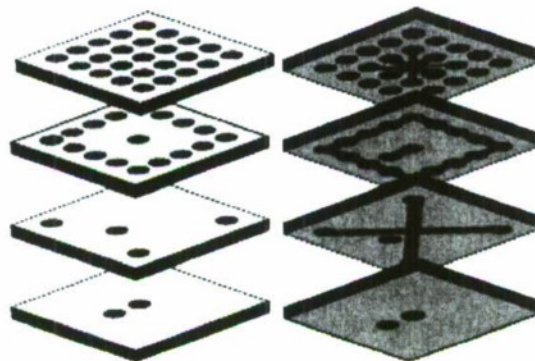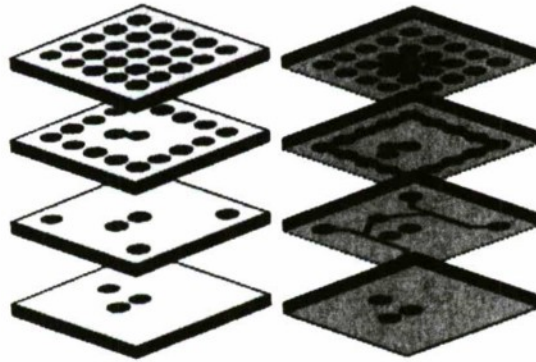**Figure 25: 3-D schematic of Distributor A**

Figure 26: 3-D schematic of Distributor B

Figure 27: 3-D schematic of Distributor C

4.4.2. Fabrication Process

The fabrication strategy requires machining of eight unique layers in four 5" DSP (double side polished) wafers, 400 μm thick, using photolithography, deep reactive ion etching and wafer bonding as key technologies. There are 4 dies per wafer (2 for distributor A, 1 for each distributor B and C). Each wafer undergoes a sequence of fabrication steps to form respective features/channels before they are bonded together to form the final distributors. The planar photomasks referred to below are found in Appendix I along with a detailed step-by-step flow chart of fabrication process (Appendix II).

4.4.2.1. Photomasks

The masks for photolithography were designed using the LayoutEditor software. Each mask design contained a set of alignment marks that will be used for proximity contact (front and back) alignment between masks and for wafer alignment prior to bonding.

Photomasks consist of a 5" polished glass plate, coated with a thin film of chromium metal. Subsequent layer of photoresist is then spun on the plate, and the exposure is made. Individual mask patterns are drawn into the photoresist coating of each photomask plates using the GCA/Mann 3600F Pattern Generator (PG). This tool exposes variably sized rotated rectangles onto the mask blank defined by a set of precision controlled moveable aperture blades. Pattern data is fractured into a format such that the entire pattern can be described by these rotated rectangles. The plate is then developed, exposing the chromium metal to be removed. Photomasks development was performed using a Hamatech Mask Plate Processor. Photomasks were then transferred to a cleaning/stripping tank containing AZ 300T solution (4% tetramethylammonium Hydroxide, 41% N-methylpyrrolidone, NMP, 1-methyl-2-pyrrolidinone, 55% propylene glycol, 1,2-propane-diol) where they were dipped for 30 minutes in order to remove remaining photoresist. The clean and patterned metal-on-glass photomasks were then rinsed with DI water and stored until needed.

Masks
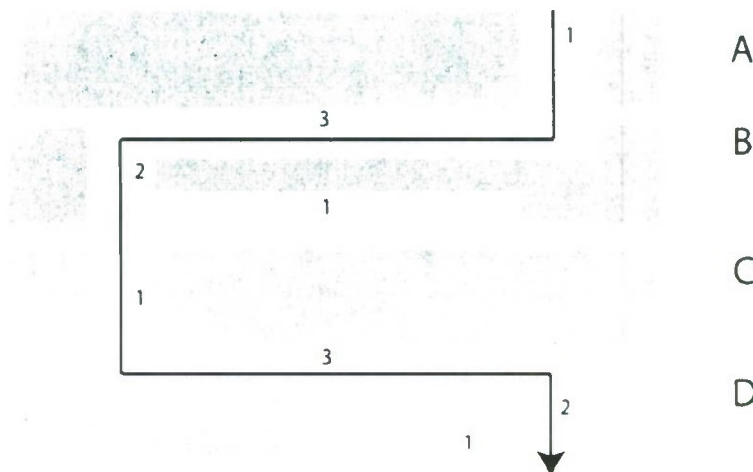
A1: Inlet holes

A

B3: Bifurcation
B2: Through-holes
B1: Bifurcation

B

C1: Through-holes

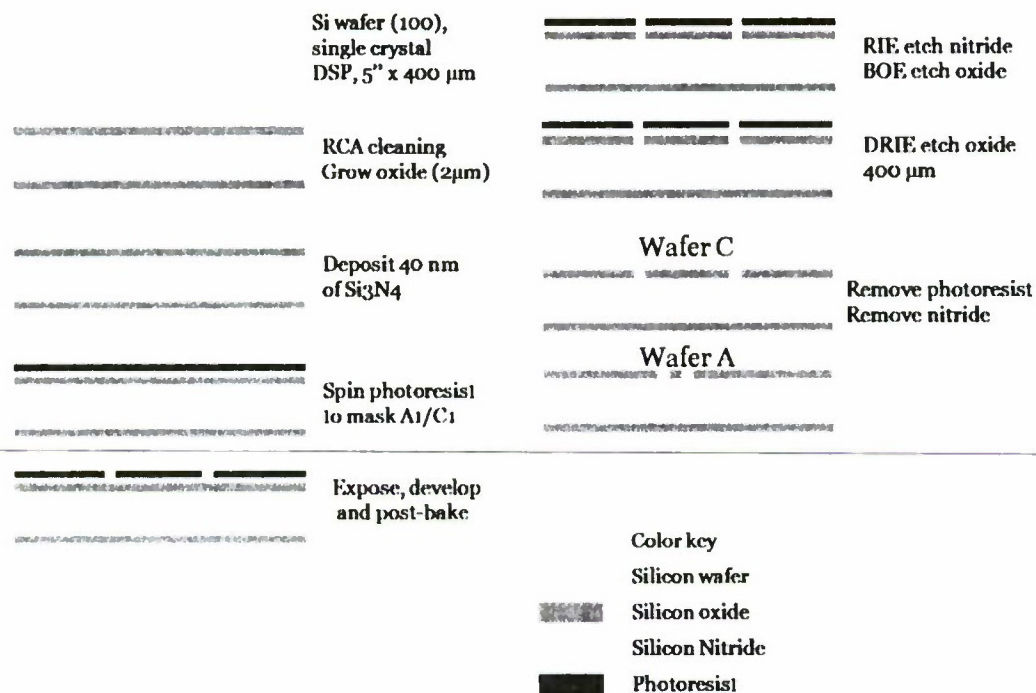C

D3: Spigots&Bifurc
D2: Spigots
D1: Monolith recess

D

Figure 28: Cross-section Schematic of assembled layers for constructing microfluidic distributors

5.4.2. Wafers A, C

Wafers A and C each contain a single pattern, comprising inlet and through-holes respectively, which is etched through the entire depth of the substrate (See Figure 28). Prior to thin film deposition, wafers are RCA cleaned to ensure an ion-and-contaminant free deposition surface. RCA cleaning process represents a standardized chemical cleansing procedure comprised of a 10 minute immersion in 1:1:5 mixture of $NH_4OH+H_2O_2+H_2O$ at 80°C to strip organic contaminants, followed by a 30 second immersion in 1:50 $HF:H_2O$ solution to remove any native oxide layer, and finally a 10 minute immersion in 1:16 $HCl:H_2O_2:H_2O$ at 80°C to remove any remaining ions from the silicon surface. The resulting cleansed silicon substrates were placed in a wet oxidation furnace in order to grow a 2 µm layer of silicon oxide, which acted as a hard-mask for subsequent patterning. Immediately after removal from the wet oxidation furnace, wafers were placed in a chemical vapor deposition system and 40 nm of silicon nitride was deposited; this layer served as an additional hard masking layer for patterning.

Application of the single photomasks for wafers A and C was accomplished as follows: In order to achieve uniform adhesion of the photoresist to the substrate, the wafer is first primed with hexamethyldisiloxane (HMDS) using a liquid primer solution (20% HMDS in propylene glycol methyl ether acetate). A 7 µm layer of thick photoresist (Shipley SPR220) is coated onto the topside of the silicon wafer by spinning at a rate of 3000 rpm for 1 min. The photoresist is then soft baked at 90°C for 1 minute on a hot plate. The resist is exposed to Mask A1/C1 by proximity contact using the EV620 contact aligner tool, exposure time was 45 seconds, wafers were then baked at 110°C for 2 hours, followed by soaking in a Tetra-methyl ammonium hydroxide (TMAH) developing solution under mild agitation until all UV-exposed photoresist

was observed to dissolve (~ 2 minutes). Wafers with fully developed photomasks where finally rinsed with DI water and spun dry. Once the photomask is applied and patterned, the underlying silicon nitride and silicon oxide hard-masks are developed using chemical etching. Silicon nitride was etched via reactive ion etching (RIE) using CF4 etchant. Unaxis 770 deep reactive silicon etcher is then used to etch 400 μm deep patterns of silicon to make the through holes. The underlying oxide/nitride layer provides and etch stop for this process. Photoresist is stripped by double dipping wafers in a hot-bath (AZ300T solution) and the silicon nitride is stripped using a hot phosphoric acid bath. At this point, wafers are ready for bonding. The underlying oxide layer is retained until immediately prior to wafer bonding in order to prevent contamination of the silicon bonding surfaces by particulates. Figure 29 shows a schematic representation of silicon fabrication steps of wafers A and C.

Si wafer (100), single crystal DSP, 5" x 400 μm

RIE etch nitride
BOE etch oxide

RCA cleaning
Grow oxide (2μm)

DRIE etch oxide
400 μm

Deposit 40 nm of Si3N4

Wafer C

Remove photoresist
Remove nitride

Spin photoresist to mask A1/C1

Wafer A

Expose, develop and post-bake

Color key
Silicon wafer
Silicon oxide
Silicon Nitride
Photoresist

Figure 29:Schematic of microfabrication process for through holes (wafers A, C)

4.4.2.3. Wafers B, D

Wafers B and D require a nested mask in order to simultaneously form the front-side bifurcation structure and the embedded through-holes which provide fluidic connection to the backside bifurcation network in a single etching step. This is accomplished by using the silicon oxide layer as a hard-mask (patterned to masks B1 and D1) in tandem with a thick photoresist layer patterned to mask B2 and D2.

Fabrication steps (schematically represented in Figure 30) are as follow: Fresh wafers are first cleaned using the RCA process (detailed above) and subsequently a 2 μm silicon oxide coating is thermally grown and an outer 40 nm silicon nitride film deposited, in identical fashioned to A/C wafers.

The silicon nitride/silicon dioxide hard mask is first patterned as follows: a Shipley S18B thin photoresist is spun on the wafers (3000 rpm, 1 min), soft baked at 90°C for 1 min, exposed to photomasks for 2 seconds, soaked in TMAH for 90 seconds or until all exposed features are dissolved, then hard-baked at 110°C for 1 min. The resulting wafers have bifurcation patterns (B1/D1) patterned in the silicon nitride/oxide hard mask. A second thick photoresist is applied to pattern the through holes (B2/D2). Photoresist Shipley SPR 220, 7 μm thick is spun coated onto the wafer. Subsequently EV620 contact aligner tool is used to align previously patterned B1/D1 and new mask B2/D2. Figure 31(a) shows alignment marks used for front contact alignment for masks B1/D1 with B2/D2. Develop and post bake. At this point, the exposed silicon is etched to a depth of 135 μm, forming the through-holes (B2/D2) which will ultimately connect the front and back-side bifurcation patterns. The thick photoresist is then stripped, exposing the silicon nitride/oxide hard mask. The exposed silicon (now patterned to the front bifurcation pattern, mask B1/D1) is etched an additional 135 μm. This second etch then forms the front bifurcation pattern to a depth of 135 μm, while completing the etching of the second through-hole pattern to a depth of 270 μm. Wafers are subsequently stripped and cleansed by double dipping wafers in a hot-bath (AZ300T solution); the front of the wafers are then coated with 750 nm of SiO_2 via PECVD, which provides an etch-step for the third etching step.

The wafers are then flipped and the backside is coated with Shipley SPR 220 thick resist, patterned to D3/B3 photomasks. Underlying silicon nitride and silicon dioxide were etched via reactive ion etching (RIE) using CF_4 and CHF_3/O_2 etchant respectively. Wafers are then DRIE etched until the embedded through-wafer vias appear in the backside features, indicating that etch has reached the SiO_2 etch stop. Then the resist is stripped and the backside and frontside silicon nitride is removed via RIE. Backside alignment mars for aligning mask B3/D3 with the front side pattern is shown in Figure 31(b). Both front and backside alignment marks shown in Figure 31 are patterned on either side of wafer. By placing these 2-point alignment marks the rotation error can be corrected.
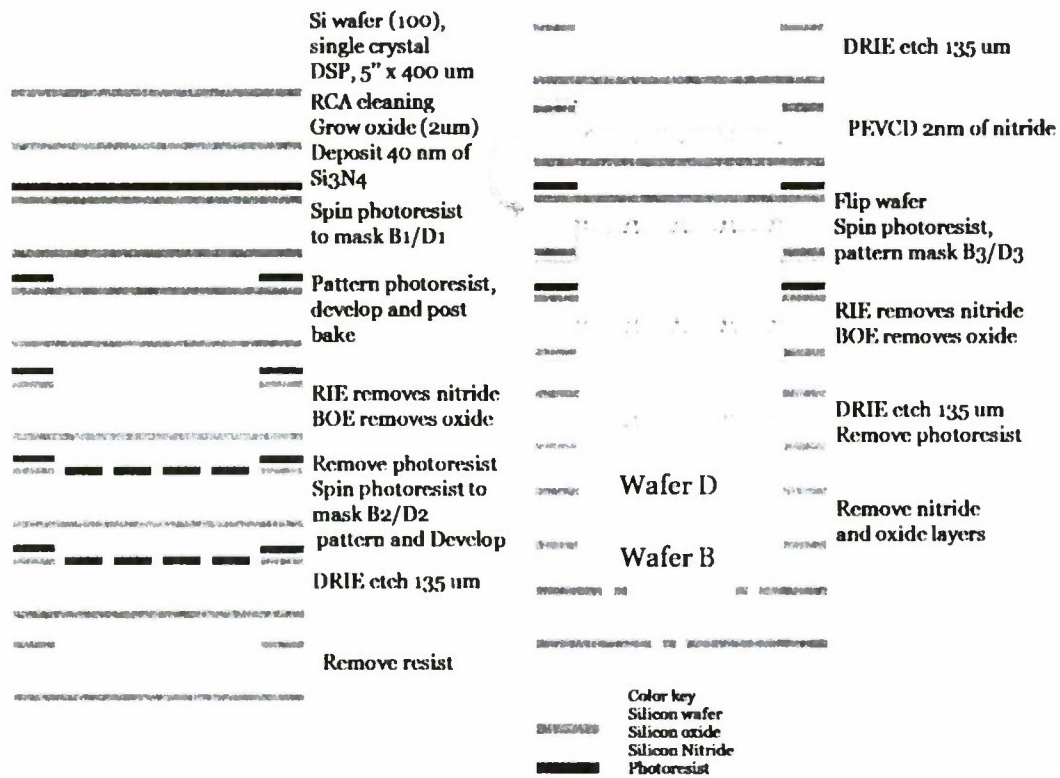
Si wafer (100),
single crystal
DSP, 5" x 400 um

DRIE etch 135 um

RCA cleaning
Grow oxide (2um)
Deposit 40 nm of
Si3N4

PEVCD 2nm of nitride

Spin photoresist
to mask B1/D1

Flip wafer
Spin photoresist,
pattern mask B3/D3

Pattern photoresist,
develop and post
bake

RIE removes nitride
BOE removes oxide

RIE removes nitride
BOE removes oxide

DRIE etch 135 um
Remove photoresist

Remove photoresist
Spin photoresist to
mask B2/D2
pattern and Develop

Wafer D

Remove nitride
and oxide layers

Wafer B

DRIE etch 135 um

Remove resist

Color key
Silicon wafer
Silicon oxide
Silicon Nitride
Photoresist

Figure 30:Schematic cross section of microfluidic distributor fabrication sequence
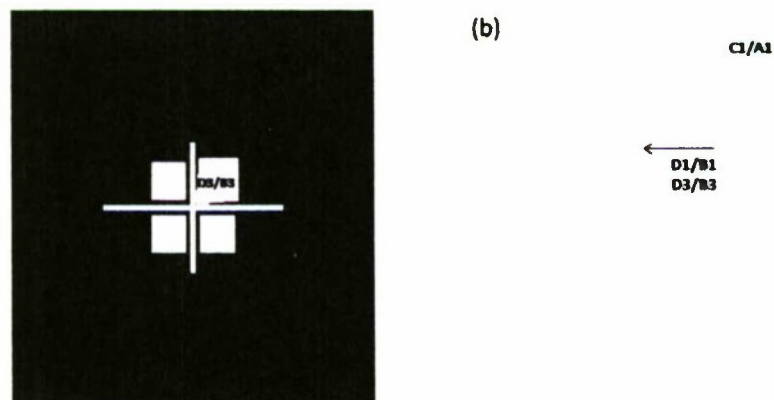
(b)

C1/A1

D3/B3

D1/B1
D3/B3

Figure 31:Alignment marks for (a) contact proximity, (b) back side alignment

4.4.2.4. Wafer Bonding

The key to successful silicon fusion bonding (SFB) (Miki et al., 2003; Schmidt, 1998) is to maintain smooth and particle free surfaces throughout processing. The silicon oxide layers provided a shielding sealing coat to protect the original Si bonding surfaces. After all wafer etches were completed (Figure 32) and ready for bonding, silicon oxide layer is removed using buffered oxide etchant (BOE) for 30 minutes. Wafers were then immediately rinsed with DI water and bonded to minimize particle deposition on the wafer surface and therefore maximize adhesion.
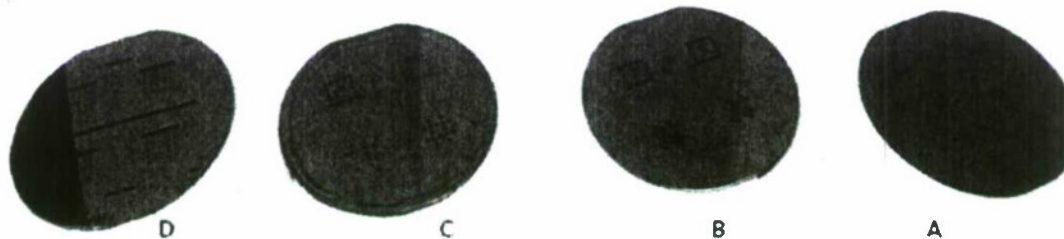
Figure 32:Actual microfabricated silicon wafers

Wafer contacting was performed by using a Suss SB8e Substrate Bonder. The bonding approach was as follows: First, all four wafers were manually aligned and contacted to form a 4 wafer stack. The stack was then placed under pressure and heat (500°C, 4 bars) in the bonder under inert atmosphere. Manual alignment was used because of the unavailability of an optical alignment chuck at the CNF. In the future we will recommend a mechanical alignment method to greatly improve this step. The initial bonding step achieves a reversible adhesion between wafers; therefore in order to achieve a permanent annealing/adhesion of the layers to form the final stack, pre-bonded stacks are subsequently placed in annealing furnace for 4 h at 1100°C.

The resulting 1.6 mm wafer stack is then die sawed using a Disco Abrasive System Model DAD-2H/6T die saw. Ideally, 4 separate distributors would be obtained from each wafer stack. During this first microfabrication experience, near 65% yield was obtained.


Figure 33:(a) Wafer stack with 4 dies, (b) resulting chip

4.4.3. Experimental

The microreactor is comprised of two silicon distributors, sealed to either end of the extruded ceramic microchannel network via compression chuck (Figure 34). Fluidic connections consist of Peek tubes of 1/16" diameter attached to a square acrylic plate that serves as an interface to properly place peek tubes in inlet and outlets diameters. Acrylic plates were then glued to the silicon distributors by using a 2-part epoxy glue.

For this study, three different distribution patterns (Figure 25-28) were employed to evaluate the flow distribution using the silicon prototypes. The ceramic microchannel networks were prepared in the same fashion explained in Section 3. The microchannel network was assembled by compression-sealing of silicon distributors to either end of the extruded ceramic microchannel network as follows. Graphite gasket sheets (1/16", McMaster-Carr) were placed in the recessed face of each silicon distributor, followed by either end of the ceramic network. Compression sealing was accomplished by a four-point compression chuck placed around the assembly and tightened by hand.
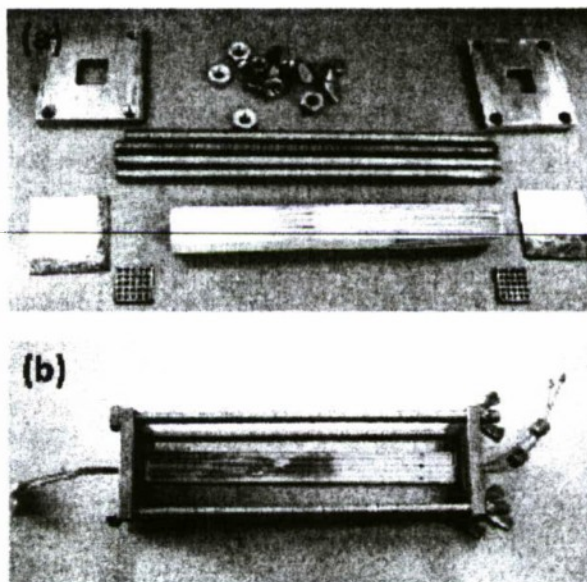

Figure 34: Distributor-packaged ceramic microchannel network; (a) unassembled portable reactor system showing two distributors, ceramic microchannel network (5x5). Graphite gaskets and compression chuck; (b) assembled view.

In order to evaluate the functionality of the silicon distributors, and the overall assembly, combustion channel flow rate was started at 0.2 SLPM then increased up to 0.5 SLPM. Thermal images were obtained during steady autothermal operation using an FLIR Thermacam™ infrared camera. By operating the reactor in the complete absence of any insulation, accurate thermal profiles of the reactor are obtained. Figure 35 shows uncalibrated thermal images taken at three

different combustion flow rates. Once flame was stable, reforming flow was introduced in the system. Thermal images taken at 3 different sets of combustion and reforming flow rates are presented in Figure 36.
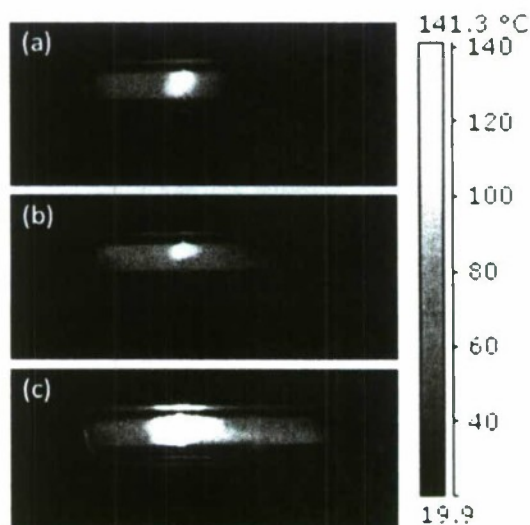
Figure 35:Thermal images corresponding to three different combustion flow rates (a) 0.2 SLPM, (b) 0.4 SLPM, (c) 0.5 SLPM
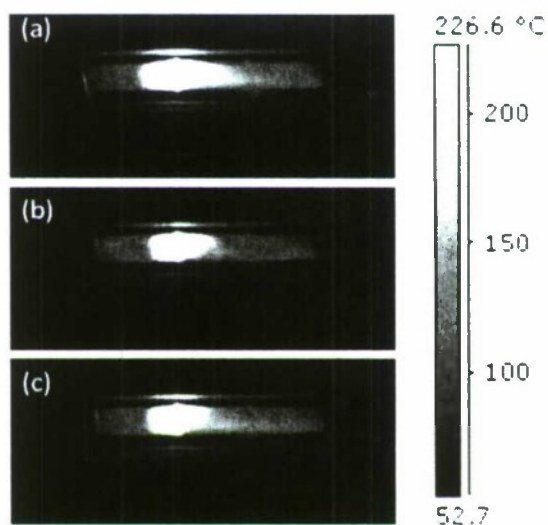
Figure 36:Thermal images corresponding to three different combustion and reforming flow rates (a) F_{comb}=0.5SLPM, F_{ref}=0.5SLPM; (b) F_{comb}=0.5SLPM, F_{ref}=0.7SLPM, (c) F_{comb}=0.5SLPM, F_{ref}=1.0 SLPM

4.4.4. Discussion

From Figure 35 and 36, flow non uniformity through the entire network is observed as combustion flame is forming only in the upper channels. As the flow rate is increased, flame spreads out through the entire network increasing the pressure drop. No flow was observed at the outlet distributor, and a visible leak appeared between the ceramic end and the silicon distributor. This leak could be attributed to flow constrictions such as graphite gaskets, small channel diameter, misalignment and glue in the features that would block the channels. In addition, sealing the ceramic network to the silicon distributors was very challenging because the monolith recess was not deep enough, leaving limited room for a gasket, therefore, the monolith ends need to be perfectly polished to achieve a good contact with the silicon wafers; but even with a perfect monolith end sealing represents a challenge. However, these preliminary findings have uncovered a critical number of refinements that are expected to result in similar performance to brass distributors.

One important thing that can be highlighted from the thermal images is that despite the flow maldistribution, hot spot is located in the center of the ceramic monolith, keeping the distributors at room temperature thus avoiding future problems with the glue method employed to attach the fluidic connections to silicon distributors.

Different chips were evaluated at both ends of the ceramic network, but only one chip corresponding to Distributor A was functional. The rest of the chips did not allow any flow through the channels and it would require high pressure to push flow through the silicon distributors.

By Si-MEMS the overall weight and volume of the distributors have drastically reduced. See Figure 37 where both brass and silicon prototypes are compared. The initial brass prototype had a weight of 690 g while the silicon distributors with a weight of 10 g exhibit a weight reduction of a factor of 98.5%

Precision-Machined Brass Plates

Lithography-Patterned Silicon Substates
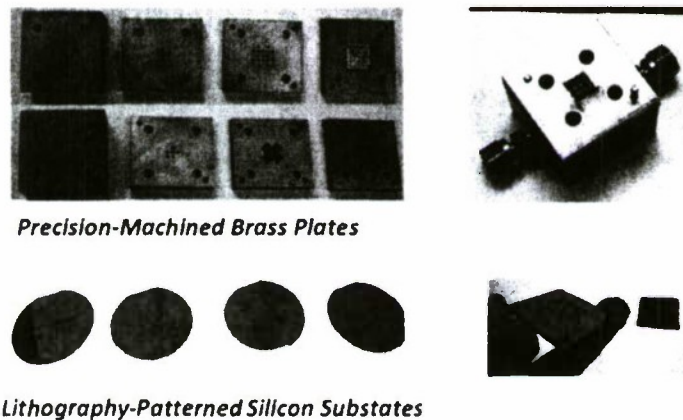
Figure 37:Comparison of overall size between brass and silicon distributors

4.4.4. Conclusions

Microelectromechanical systems (MEMS) and silicon technology are promising technologies for miniaturizing conventional macro-scale distributors into compact devices. See Appendix III for the projected energy density using the silicon packaged ceramic microchannel network.

From the first micromachining experience building the silicon distributors, a 6% final packaged device yield was obtained, as only one of the distributor prototypes was functional. However, the main goal of achieving miniaturization of flow distributors by reducing weight and volume was accomplished. More importantly, this first effort has identified the key refinements to design and experimental method for the continued development of this technique. This low yield can be attributed to notable design challenges for complex MEMS in addition to the lack of previous operating experience.

Based on the experience gained with the microfabrication of the first generation of silicon distributors, the following suggestions are made for next generation of silicon distributors:

i. Contact all four silicon wafers together using alignment pins for accurate wafer positioning.
ii. In order to improve the bonding between wafers, it is recommended to clean organic residues from wafer surfaces with piranha solution (mixture of sulfuric acid (H_2SO_4) and hydrogen peroxide (H_2O_2)), after BOE stripping and immediately before contacting.
iii. Design front wafer with a deeper monolith recess. This would allow proper seating of a sealing gasket between the silicon and ceramic monolith. This could be achieved by using a thicker silicon substrate (e.g. 2 mm)
iv. Design spigots with 1/16" diameter instead of 1/32". This would reduce the pressure drop in the system and would allow flow through the outlet distributor more easily.
v. Position inlets and outlets with a larger distance in order to obtain an optimum positioning and gluing of fluidic connections; alternately, replace the hard-glue with a solder-fitting technique (Wilhite, 2009).
vi. Apply even pressure when hand tightening compression chuck. A small scratch on the silicon surface may easily spread over the whole body under the influence of mechanical strain.

Further improvements of the microfabrication steps will enable the construction of more functional distributors that will be employed for the demonstration of the heat integration between methanol combustion and steam reforming of methanol for the autothermal production of hydrogen.

5. Technology Transfer

None.

6. Refereed Journal Articles (4 accepted, 1 in review)

1. G.S. Honda and **B.A. Wilhite**[†],"The Impact of Externally Applied Thermal Gradients on Catalyst Behavior in Wall-Coated Microreactors," *submitted to Chemical Engineering Science.*

2. A. Moreno, S. Damodharan and **B.A. Wilhite**[†], "Influence of Two-Dimensional Distribution Schemes upon Reactor Performance in a Ceramic Microchannel Network for Autothermal Methanol Reforming," *special ISCRE-21 Issue, Industrial & Engineering Chemistry Research.*

3. D. Kim*, D. Donohue[‡], B. Kuncharam*, C. Duval[‡] and **B.A. Wilhite**[†], "Towards an Integrated Ceramic Micro-Membrane Network," *special ISCRE-21 Issue, Industrial & Engineering Chemistry Research.*

4. A. Moreno and B.A. Wilhite. "Autothermal Hydrogen Generation from Methanol in a Ceramic Microchannel Network". *Journal of Power Sources.* 195, 1964-1970, 2010.

5. A. Moreno, K. Murphy, B.A. Wilhite. "Parametric study of solid-phase axial heat conduction in thermally integrated microchannel networks". *Ind. Eng. Chem. Res.,* 47 (23), 9040-9054, 2008.

7. Books and Chapters (1)

Wilhite, B. A., 2009. Thermal Management, in: Mitsos, A., Barton, P. I. (Eds), Microfabricated Power Generation Devices: Design and Technology. New York, Wiley-VCH.

8. Technical Reports (0)

None to-date.

9. Presentations (14)

1. *B.A. Wilhite, "Microchemical Systems for Portable Biofuels Reforming: Revisiting and Rethinking Chemical Reaction Engineering Analysis," *Session in Honor of Arvind Varma's 60th Birthday, AIChE 2007 annual meeting,* November 5th, 2007.

2. *B.A. Wilhite, "Microchemical Systems for Portable Biofuels Reforming," *presented at Department of Chemical Engineering, West Virginia University,* February 22nd, 2008.

3. *B.A. Wilhite, "Fuel Cells: Powering a Sustainable Future," presented at the University of Connecticut Sustainable Energy Symposium, March 31st, 2008.

4. *B.A. Wilhite, "Microchemical Systems for Portable Biofuels Reforming: Revisiting and Rethinking Chemical Reaction Engineering Analysis," *India-US Symposium on Energy and Sustainability, Hosted by ChemCon 2008,* Chandigarh, India, December 29th, 2008.

5. *B.A. Wilhite, "Multifunctional Reactors and Materials," *presented at Department of Chemical Engineering, Cornell University, September 21st, 2009.*

6. * **B.A. Wilhite**, "Hot-Spots in Chemical Reaction Engineering – Multifunctional Reactors and Materials," *presented at the Frontiers of Chemical Reaction Engineering invited session at the 2009 AIChE Annual Meeting in Nashville, TN.*

7. A.M. Moreno and **B.A. Wilhite,** "2-D Complex Flow Distribution Schemes for Autothermal Hydrogen Production from Methanol," poster presentation at 21st International Symposium on Chemical Reaction Engineering (ISCRE-21), abstract 198 (2010).

8. D. Kim, D. Donohue and **B.A. Wilhite,** "Integrated Ceramic Micro-Membrane Networks for Hydrogen Production from Ethanol," oral presentation at 21st International Symposium on Chemical Reaction Engineering (ISCRE-21), abstract 197 (2010).

9. G. Honda[‡] and **B.A. Wilhite,** "The Effect of Catalyst Layer Thermal Gradients on Catalyst Efficiency in Wall-Coated Microreactors," presented at 2009 AIChE Annual Meeting, 82d, November 9th, 2009.

10. A.M. Moreno and **B.A. Wilhite,** "Autothermal Hydrogen Generation from Methanol in a Ceramic Microchannel Network," presented at 2009 AIChE Annual Meeting, 522b, November 12th, 2009.

11. A. Moreno, G. Honda[‡], D. Kim and **B.A. Wilhite**, "Design Strategy for Thermally Integrated Ceramic Microreactor Networks," *presented at 8th World Congress of Chemical Engineers (WCCE 8), Montreal, QC, August 26th, 2009.*

12. **B.A. Wilhite**[*]and A. Moreno, "Heat-Integrated Hydrogen Production from Liquid Fuels: Demonstration of Cartridge-Based Micro-Reformers," *presented at 238th Annual Meeting of the American Chemistry Society, FUEL 37, Washington D.C., August 16th, 2009.*

13. *A. Moreno and **B.A. Wilhite,** "Experimental Demonstration of a Thermally-Integrated Microchannel Network," *presented at 2008 AIChE Annual Meeting, 423d, November 19th 2008.*

14. *A. Moreno and **B.A. Wilhite,** "Modeling of a Micro-Scale Heat Exchanger Reactor for Portable Hydrogen Production," *presented at American Institute of Chemical Engineers (AIChE) Annual Meeting, Salt Lake City, UT, 37a (2007).*

11. Patents (1)

1. Wilhite, B.A., Moreno, A., D. Kim, "Process Intensification in Microreactors," provisional patent application Serial No. 61/001,578 (2008).

12. Honors/Awards/Prizes (0)

None to-date.

13. Related Sponsored Work (3)

- "Hydrogen from Ethanol via Integrated Ceramic Microchannel Membrane Networks," PI: Benjamin A. Wilhite. National Science Foundation, Chemical and Transport Science Division. Award Amount, $239,000. Award Period: 06/01/07 – 05/31/10.
- "Integrated Fuel Reformers for Hydrogen Production from Green Resources," P.I: Benjamin A. Wilhite. DuPont de Nemours Coorporation, Young Professor Grant. Award Amount, $75,000. Award Period: 09/01/07 – 08/30/10.

- "Analysis of Hydrogen Purification Membranes for Use in Fuel Cell-Based Naval Power Systems," P.I.: Benjamin A. Wilhite. Office of Naval Research. Award Amount, $97,055. Award Period: 01/01/08 – 12/31/08.

REFERENCES

Amador, C., Gavrilidis, A., Angeli, P., 2004. Flow Distribution in Different Microreactor Scale-out Geometries and the Effect of Manufacturing Tolerances and Channel blockage, Chem. Eng. J. 101, 379.

Geankopolis, C., 2003. Transport Processes and Separation Process Principles New Jersey: Prentice Hall.

Kim, D., Kellogg, A., Livaich, E., Wilhite, B. A., 2009. Towards an integrated ceramic micro-membrane network: Electroless-plated palladium membranes in cordierite supports Journal of Membrane Science 340(1-2), 109-116.

London, A. P., Ayón, A. A., Epstein, A. H., Spearing, S. M., Harrison, T., Peles, Y., Kerrebrock, J. L., 2001. Microfabrication of a high pressure bipropellant rocket engine, Sensors and Actuators A: Physical 92(1-3), 351-357.

Miki, N., Zhang, X., Khanna, R., Ayón, A. A., Ward, D., Spearing, S. M., 2003. Multi-stack silicon-direct wafer bonding for 3D MEMS manufacturing, Sensors and Actuators A: Physical 103(1-2), 194-201.

Mirza, A. R., Ayon, A. A., 1999. Silicon wafer bonding for MEMS manufacturing, Solid State Technology 42(8), 73.

Moreno, A. M., Murphy, K., Wilhite, B. A., 2008. Parametric Study of Solid-Phase Axial Heat Conduction in Thermally Integrated Microchannel Networks, Ind. Eng. Chem. Res. 47, 9040.

Moreno, A. M., Wilhite, B. A., 2010. Autothermal hydrogen generation from methanol in a ceramic microchannel network Journal of Power Sources 195(7), 1964-1970.

Peterson, R., 1999. Numerical Modeling of Conduction Effects in Microscale Counterflow Heat Exchangers, Microscale Thermophysical Engineering 3, 17.

Schmidt, M. A., 1998. Wafer-to-wafer Bonding for Microstructure Formation, Proceedings of the IEEE 86(8), 1575.

Stief, T., Langer, O. U., Schubert, K., 1999. Numerical Investigations of Optimal Heat Conductivity in Micro Heat Exchangers, Chem. Eng. Technol. 21(4), 297.

Wada, Y., Schmidt, M. A., Jensen, K. F., 2006. Flow Distribution and Ozonolysis in Gas-liquid Multichannel Microreactors Industrial & Engineering Chemistry Research 45, 8036.